J. Fluid Mech. (2023), *vol*. 975, A13, doi:10.1017/jfm.2023.824

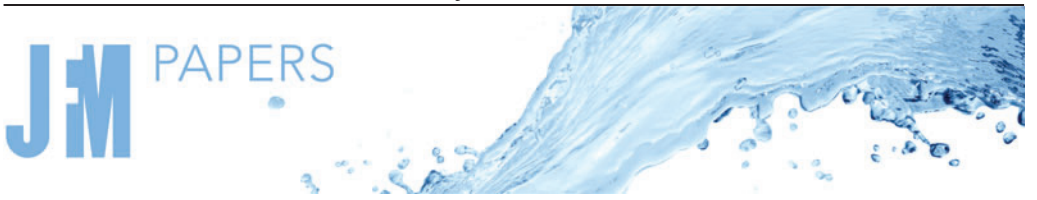

Hierarchy of coherent vortices in turbulence behind a cylinder

Jun Fujino[1], **Yutaro Motoori**[1],† **and Susumu Goto**[1],†

[1]Graduate School of Engineering Science, Osaka University, 1-3 Machikaneyama, Toyonaka, Osaka 560-8531, Japan

(Received 6 March 2023; revised 23 September 2023; accepted 24 September 2023)

To draw concrete pictures of the hierarchy of multiscale coherent vortices in turbulence behind a cylinder and to reveal their sustaining mechanism, we conduct direct numerical simulations of the turbulence at the Reynolds number, which is defined by the uniform inflow velocity and the cylinder diameter, 5000. The turbulence consists of three kinds of hierarchies of coherent vortices in three distinct regions: namely, the downstream region, the recirculation region just behind the cylinder and the separate shear layers. By tracking the temporal evolution of multiscale vortices in each of these regions, we demonstrate that, in all the three regions, smaller coherent vortices tend to align in the direction perpendicular to larger ones. This implies that smaller vortices are stretched and amplified in the strain-rate fields around larger ones. We also show the relevance of this observation to the energy cascade. Smaller-scale vortices receive the kinetic energy in the regions where they are stretched by larger-scale vortices; and, at the same time, they tend to compress larger ones, thus reducing larger-scale kinetic energy.

Key words: wakes

1. Introduction

One of the most important unsolved issues on turbulence is to elucidate the energy cascade. Many researchers have accumulated many pieces of knowledge on the energy cascade in turbulence through various analyses from multifaceted perspectives. First, it is evident that the kinetic energy cascades, on average, from large to small scales in turbulence. This was verified in studies on the energy flux in wavenumber space (e.g. Domaradzki & Rogallo 1990; Ohkitani & Kida 1992; Borue & Orszag 1998; Cerutti & Meneveau 1998; Chen *et al.* 2003; Aoyama *et al.* 2005) and in a scale space defined

† Email addresses for correspondence: y.motoori.es@osaka-u.ac.jp, s.goto.es@osaka-u.ac.jp

© The Author(s), 2023. Published by Cambridge University Press. This is an Open Access article, distributed under the terms of the Creative Commons Attribution licence (http://creativecommons.org/licenses/by/4.0), which permits unrestricted re-use, distribution and reproduction, provided the original article is properly cited.

https://doi.org/10.1017/jfm.2023.824 Published online by Cambridge University Press

by the two different locations in turbulence (e.g. Cerutti & Meneveau 1998; Yasuda & Vassilicos 2018). However, there is no clear consensus on the energy transfer mechanism in the instantaneous turbulent fields. In fact, although various analyses concluded that interscale energy transfer can occur bidirectionally (e.g. Borue & Orszag 1998; Cerutti & Meneveau 1998; Tao, Katz & Meneveau 2002; Chen *et al.* 2003; Aoyama *et al.* 2005; Gomes-Fernandes, Ganapathisubramani & Vassilicos 2015; Alves Portela, Papadakis & Vassilicos 2017; Yasuda & Vassilicos 2018), we do not fully understand the relevance of these observations to the energy cascade. Here, we refer to some of the commonly used methods for quantifying energy transfer. Studies on large eddy simulations (LES) often quantify interactions between grid-resolved and subgrid scales to examine, for example, their relationship to coherent flow structures (e.g. Piomelli, Yu & Adrian 1996; Lin 1999; Natrajan & Christensen 2006; Hong *et al.* 2012; Watanabe, Da Silva & Nagata 2020). There are also quite a few studies (e.g. Marati, Casciola & Piva 2004; Cimarelli, De Angelis & Casciola 2013; Gomes-Fernandes *et al.* 2015; Hamba 2015; Cimarelli *et al.* 2016; Yasuda & Vassilicos 2018; Hamba 2019; Zhou *et al.* 2020) arguing the interscale energy transfer by using the Kármán–Howarth–Monin–Hill (KHMH) equation (Hill 2002). For instance, in turbulence behind an obstacle, which is also the target of the present study, Alves Portela *et al.* (2017) demonstrated that the energy transferred to larger scales in the mainstream direction. In their subsequent study (Alves Portela, Papadakis & Vassilicos 2020), they also showed the energy flux to small-scale turbulence due to the largest-scale coherent structures. In addition to studies on LES and those using the KHMH equation, there are also studies on interscale interactions of turbulence (Kawata & Alfredsson 2018, 2019; Chan, Schlatter & Chin 2021) by the spectral analyses of the scale-decomposed Reynolds stress. These studies have contributed to turbulence models and theories (e.g. Kobayashi 2005; Kobayashi, Ham & Wu 2008; Marusic & Monty 2019; Vela-Martín 2022). However, as mentioned above, it is still unclear how the energy is transferred between different scales in physical space. This is because the energy fluxes and transfers defined in most of the aforementioned studies denote the amounts of energy passing across a scale per unit time and its derivative with respect to scale, respectively. Hence, these quantities, in general, cannot capture the energy transfers between two scales. An important point of the present study is to quantify the energy flux between two scales, which may be estimated locally in space, to clarify the concrete picture of the energy cascade.

We also investigated the generation mechanism of the hierarchy of coherent vortices in turbulence. For turbulence in a periodic cube, not only our group (e.g. Goto 2008, 2012; Goto, Saito & Kawahara 2017) but also many authors (e.g. Leung, Swaminathan & Davidson 2012; Cardesa, Alberto & Jiménez 2017; Doan *et al.* 2018; Hirota *et al.* 2020) identified vortical structures with various sizes by decomposing turbulent fields obtained by the direct numerical simulations (DNS) into different scales. Such a scale decomposition gives a clear picture of the hierarchy of coherent vortices. For example, Goto *et al.* (2017) showed that at each level of the hierarchy, coherent tubular vortices tend to form counter-rotating pairs. Since the counter-rotating vortex pairs induce a strong strain-rate field around them, they effectively amplify smaller-scale vortices (Goto 2012; Goto *et al.* 2017) due to vortex stretching. It is also evident that small-scale vortices tend to be generated by being stretched by twice to eight times larger vortices (Leung *et al.* 2012; Goto *et al.* 2017). Recently, Yoneda, Goto & Tsuruhashi (2022) quantified the spatially averaged interscale energy transfer due to the vortex stretching. Under the assumptions based on the generation mechanism of the hierarchy of vortices, they also derived the $-5/3$ power law of the energy spectrum without Kolmogorov's similarity hypotheses. Thus, these results are not inconsistent with the conclusion that the scale-local vortex stretching

https://doi.org/10.1017/jfm.2023.824 Published online by Cambridge University Press

is the cause of the energy cascade. Incidentally, the scale decomposition of turbulence also revealed the multiscale nature in near-wall turbulence (e.g. Lozano-Durán, Holzner & Jiménez 2016; Lee, Sung & Zaki 2017; Motoori & Goto 2019, 2021). In turbulent boundary layers (Motoori & Goto 2019) and turbulent channel flow (Motoori & Goto 2021), we observed similar energy cascading events for vortices at small scales, i.e. vortices smaller than the Corrsin length scale (Corrsin 1958) in the log layer.

The present study aims to elucidate (i) the concrete picture of the hierarchy of coherent vortices in the turbulent wake behind a cylinder and (ii) the sustaining mechanism of these vortices. Here, we must note that the sustaining mechanism of the large-scale vortices, which are the origins of the energy cascade, can be different from that in turbulence without flow separation, for example, periodic turbulence (Goto *et al.* 2017), zero-pressure-gradient turbulent boundary layers (Motoori & Goto 2019) and turbulent channel flow (Motoori & Goto 2021). We must also note that the flow state behind a cylinder is different depending on the ranges of the Reynolds number $Re_D = U_\infty D/\nu$ (Williamson 1996; Forouzi Feshalami *et al.* 2022), where U_∞ is the upstream uniform velocity magnitude, D is the diameter and ν is the kinematic viscosity of the fluid. For $Re_D \approx 50$–190, Kármán vortices are shed alternately from the cylinder. The laminar-turbulence transition occurs for $Re_D \approx 190$–260, where streamwise rib vortices are formed between roller vortices, which correspond to the Kármán vortices at low Re_D. In this regime two modes are known. For $Re_D \approx 190$–230, roller vortices are deformed to tongue-shaped vortex sheets (mode A), whereas, for $Re_D \approx 230$–260, they stretch and amplify smaller rib vortices around themselves (mode B). In the turbulent regime $Re_D \approx 10^3$–2×10^5, small vortices emerge in the separated shear layers due to the Kelvin–Helmholtz (KH) instability. In particular, for $Re_D \lesssim 6000$, the vortices generated through the KH instability are advected into the downstream shear layer while keeping their shape. In contrast, for $Re_D \gtrsim 6000$, the KH vortices are deformed in the upstream shear layer due to the earlier transition to developed turbulence (e.g. Norberg 2003; Rajagopalan & Antonia 2005; Thompson & Hourigan 2005). For the further developed turbulence for $Re_D \approx 2 \times 10^5$–$10^6$, the separated shear layer reattaches to the cylinder, leading to the well-known drag crisis.

Although the transition mechanisms in a wide range of Re_D have been extensively investigated by experiments (see the reviews by Williamson 1996; Forouzi Feshalami *et al.* 2022) and LES (e.g. Breuer 1998; Lehmkuhl *et al.* 2014; Rodríguez *et al.* 2015), there are only a few studies of DNS that focus on energy cascade and its relation to multiscale flow structures. For example, Aljure *et al.* (2017) conducted the DNS of turbulence behind a cylinder for $Re_D = 5000$ to demonstrate that the shed vortices are distorted in the axial direction (i.e. the so-called vortex dislocation). Aasland *et al.* (2022) also conducted DNS of turbulence behind a single cylinder and tandem cylinders for $Re_D = 10^4$ to investigate the reattachment mechanism of the separated shear layers. In the present study we investigate developed turbulence behind a cylinder at $Re_D = 5000$, where vortices emerge in the shear layer but they are hardly deformed. Here, we regard the present turbulence as a developed one because, as will be shown below, the power spectrum obeys a power law (see figure 2 in § 2), which implies a sufficiently large separation in scales.

In the rest of the paper we first describe the numerical methods in § 2. Then, we investigate qualitatively (§ 3) and quantitatively (§ 4) the generation mechanism of the hierarchy of multiscale coherent vortices in the three distinct regions behind the cylinder. In § 5 we investigate energy transfer in instantaneous fields to show the relevance of the generation mechanism of the hierarchy of vortices to the energy cascade.

https://doi.org/10.1017/jfm.2023.824 Published online by Cambridge University Press

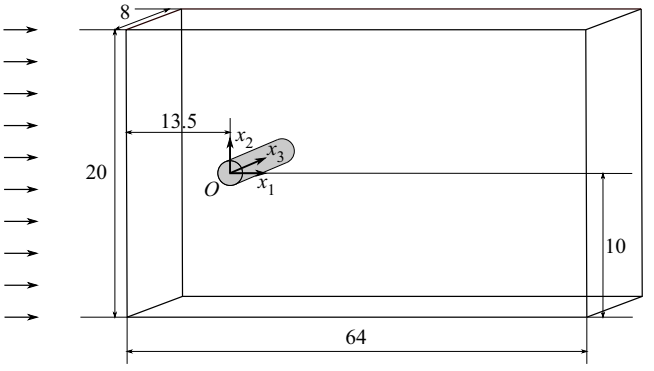

Figure 1. Numerical configuration. We set the origin of the coordinate at the cross-point of a centreline in the x_2 direction and the axis of the cylinder.

Re_D	$N_1 \times N_2 \times N_3$	$L_1 \times L_2 \times L_3$	Δt	Δ
5000	$8192 \times 2560 \times 1024$	$64 \times 20 \times 8$	6.25×10^{-4}	7.81×10^{-3}

Table 1. Numerical parameters. Here N_i is the number of grid points in the x_i direction, L_i is the domain size in the x_i direction, Δt is the time per step and Δ is the grid width.

2. Numerical methods

2.1. *Direct numerical simulations*

We conduct DNS of turbulence behind a cylinder at $Re_D = 5000$ by numerically integrating the non-dimensional forms of the Navier–Stoke equation,

$$\frac{\partial \boldsymbol{u}}{\partial t} + \boldsymbol{u} \cdot \nabla \boldsymbol{u} = -\nabla p + \frac{1}{Re_D} \nabla^2 \boldsymbol{u}, \tag{2.1}$$

and the continuity equation,

$$\nabla \cdot \boldsymbol{u} = 0, \tag{2.2}$$

of an incompressible fluid. Here, $\boldsymbol{u}(\boldsymbol{x}, t)$ and $p(\boldsymbol{x}, t)$ are the non-dimensional fluid velocity and pressure fields at position $\boldsymbol{x}$ and time t, where we use D, D/U_∞ and ρD^3 (ρ is the mass density of the fluid) as the length, time and mass units, respectively.

Figure 1 shows the numerical configuration. We define the x_1, x_2 and x_3 axes in the streamwise, the normal to the cylinder and the axial directions, respectively. We list numerical parameters of the DNS in table 1, where N_i and L_i denote the number of grid points and the side of the numerical domain in the x_i direction, respectively.

We impose the uniform flow, $\boldsymbol{u} = (1, 0, 0)$, at the inlet and the convective condition, $\partial u_i/\partial t + U_m \partial u_i/\partial x = 0$, at the exit, where $U_m(t)$ is the spatial average of the u_1 at the exit plane. Under these boundary conditions, we numerically integrate (2.1) and (2.2) by the simplified marker and cell method (see Amsden & Harlow 1970; Kajishima & Taira 2017). For the global mass conservation in the computational domain, we correct u_1 at the exit plane (Simens *et al.* 2009) before we solve the Poisson equation for the pressure. For the temporal integration, we use the second-order Adams–Bashforth method for the advection term and the second-order Crank–Nicolson method for the viscous term. We set a uniform Cartesian staggered grid, and employ the second-order central finite

https://doi.org/10.1017/jfm.2023.824 Published online by Cambridge University Press

difference to evaluate the spatial derivatives. The grid width Δ is set to be smaller than $2.6\eta(x_1, x_2)$, and the time Δt per step is smaller than $0.013\tau_\eta(x_1, x_2)$. Here, $\eta(x_1, x_2)$ and $\tau_\eta(x_1, x_2)$ are the Kolmogorov length and time, which are estimated by $(\nu^3/\bar{\epsilon})^{1/4}$ and $(\nu/\bar{\epsilon})^{1/2}$, respectively. Here, $\bar{\epsilon}(x_1, x_2)$ is the energy dissipation rate averaged over t and x_3. We express the cylinder using the immersed boundary method (Uhlmann 2005; Kempe & Fröhlich 2012) to impose the non-slip boundary condition on the surface of the cylinder. In this method we distribute Lagrangian force points uniformly on the cylinder surface with the same spacing as the grid width of the DNS. We then impose body force on the fluid grid points around the force points so that the fluid velocity at the force points satisfies the non-slip boundary condition.

In the following, we show results in the statistically steady state. We define the origin ($t = 0$) of time by the moment when about 3.42 washout times elapse since roller vortices start shedding. We take statistics for the duration $0 \leqslant t \leqslant T$ with $T = 81.24$, during which about 16 pairs of roller vortices are shed. We validate the present DNS in Appendix A.

2.2. *Scale decomposition*

We evaluate the power spectrum density,

$$E_2(\boldsymbol{x}, f) = \frac{|\widehat{u_2'}(\boldsymbol{x}, f)|^2}{T}, \tag{2.3}$$

for the x_2 component of the fluctuating turbulent velocity. Here,

$$\widehat{u_i'}(\boldsymbol{x}, f) = \int_0^T u_i'(\boldsymbol{x}, t) \exp(-2\pi \mathrm{i} f t)\, \mathrm{d}t \tag{2.4}$$

denotes the Fourier transform of $u_i'(\boldsymbol{x}, t)$. Figure 2(a) shows the mean power spectrum density of $E_2(x_1, x_2 = 0, f)$, which is averaged over x_3, at eight streamwise locations ($1 \leqslant x_1 \leqslant 8$). We see that the power spectrum densities have a peak at $f = 0.20$. This means that the Strouhal number St is 0.20 for this Re_D ($= 5000$), which is in good agreement with the value 0.203 of the DNS results at $Re = 3900$ (Parnaudeau *et al.* 2008). Incidentally, the secondary peak at $f = 3St$ observed for $x_1 \geqslant 2$ is also in good agreement with the LES results (Parnaudeau *et al.* 2008). This secondary peak was also observed in the experiment (Ong & Wallace 1996) and DNS (Lehmkuhl *et al.* 2013), though, to the best of our knowledge, its origin is unknown. We also observe an approximate $-5/3$ power law at all locations between $x_1 = 1$ and 8. We can confirm the establishment of the power law by looking at figure 2(b), where the compensated spectra $E_2 f^{5/3}$ show plateaus within a factor of 2–3. This implies that there exists a hierarchy of vortices with various sizes in this region. We cannot, however, observe such a hierarchy by using the raw data of the velocity gradients. This is demonstrated in figure 3(a), which shows the isosurfaces of the second invariant Q of the velocity gradient tensor. In this figure we can only observe fine tubular vortices with the diameter approximately 10η (see figure 8 in § 3.2). The observation that the raw values of Q only capture the smallest-scale vortices is common in many kinds of turbulence; e.g. turbulence in a periodic cube (Goto *et al.* 2017), turbulent boundary layers (Motoori & Goto 2019) and turbulent channel flow (Motoori & Goto 2021). This is because the smallest-scale vortices determine the velocity gradients. Therefore, we need a scale decomposition to observe the hierarchy of vortices.

There are many studies using scale decompositions for inhomogeneous turbulence (e.g. Lee *et al.* 2014; Hwang *et al.* 2016; Lozano-Durán *et al.* 2016; Lee *et al.* 2017; Motoori & Goto 2019, 2021). Here, we employ the Gaussian filtering method adopted by Motoori

https://doi.org/10.1017/jfm.2023.824 Published online by Cambridge University Press

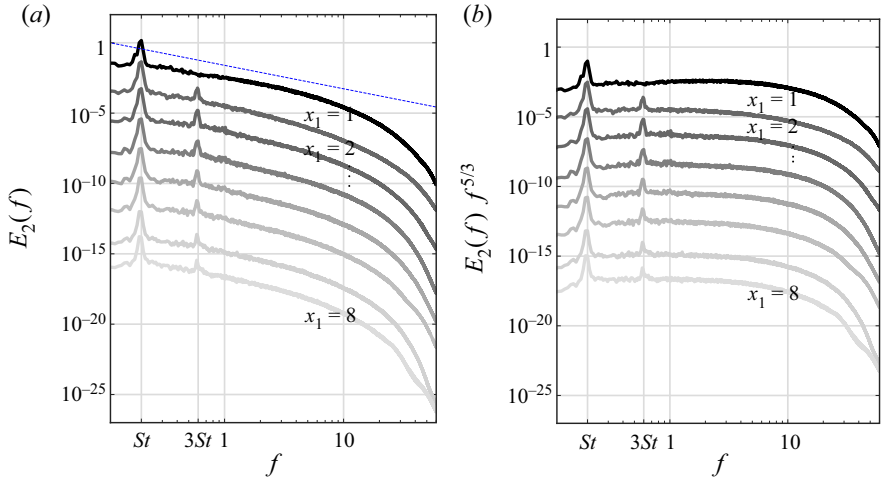

Figure 2. Power spectrum density (*a*) $E_2(x_1, x_2 = 0, f)$ and (*b*) compensated by $f^{5/3}$: $E_2(x_1, x_2 = 0, f)f^{5/3}$, both averaged over x_3 at $x_1 = 1, 2, \ldots, 8$. We have vertically shifted the curves for $x_2 \geq 2$. Blue dotted line indicates the $-5/3$ power law.

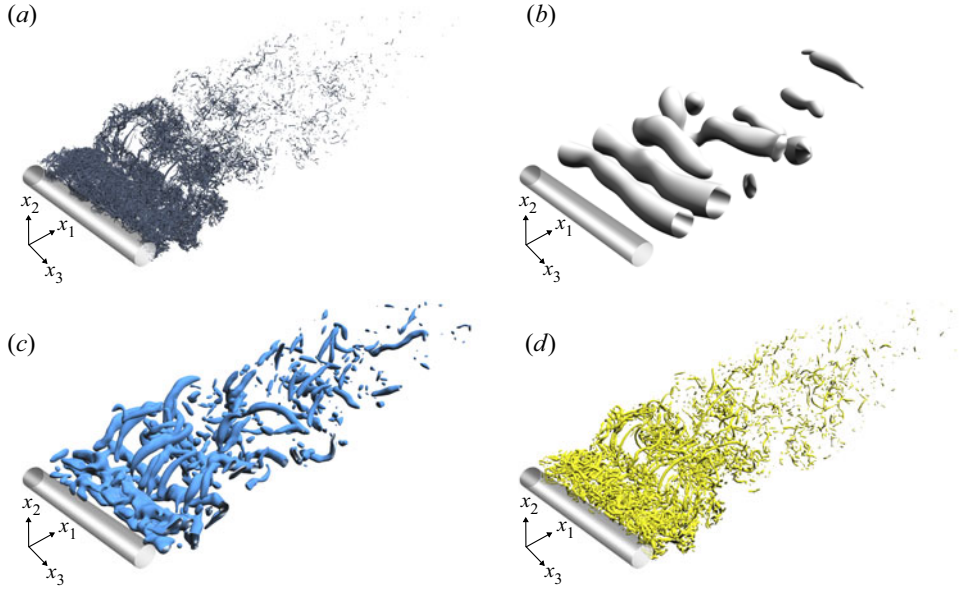

Figure 3. Coherent vortices with various sizes in the turbulent wake. (*a*) Isosurfaces of the second invariant Q' of the velocity gradient tensor. (*b–d*) Isosurfaces of the second invariant $Q'^{(\sigma)}$ of the scale-decomposed velocity gradient tensor with (*b*) filter scale $\sigma = \sigma_{max}$, (*c*) $\sigma_{max}/4$ and (*d*) $\sigma_{max}/16$. We set the thresholds in terms of the root mean square of Q'_{rms} (or $Q'^{(\sigma)}_{rms}$) at $(x_1, x_2) = (3, 0)$: (*a*) $1.53Q'_{rms}(= 75)$, (*b*) $0.60Q'^{(\sigma)}_{rms}(= 5.0 \times 10^{-3})$, (*c*) $0.50Q'^{(\sigma)}_{rms}(= 1.0 \times 10^{-1})$ and (*d*) $1.42Q'^{(\sigma)}_{rms}(= 2.0)$.

& Goto (2021) and Motoori, Wong & Goto (2022). First, we apply the three-dimensional Gaussian filter to the velocity u_i,

$$u_i^{[\sigma]}(\boldsymbol{x}, t) = \frac{1}{(\sqrt{2\pi}\sigma)^3} \int u_i(\boldsymbol{x}', t) \exp\left(\frac{-(\boldsymbol{x} - \boldsymbol{x}')^2}{2\sigma^2}\right) \mathrm{d}\boldsymbol{x}', \tag{2.5}$$

https://doi.org/10.1017/jfm.2023.824 Published online by Cambridge University Press

to obtain low-pass filtered velocity components $u_i^{[\sigma]}$. Here, σ denotes the filter width. We choose a constant σ irrespective of $\boldsymbol{x}$ because we will investigate Lagrangian tracking of vortices on given scales in § 3.1. Note that $u_i^{[\sigma]}$ only contains the velocity fields with scales larger than σ. Note also that the Fourier transform of (2.5) leads to

$$\widehat{u_i^{[\sigma]}}(\boldsymbol{k}, t) = \widehat{u_i}(\boldsymbol{k}, t) \exp\left(\frac{-|\boldsymbol{k}|^2\sigma^2}{2}\right), \tag{2.6}$$

where $\hat{X}(\boldsymbol{k})$ denotes the Fourier transform of $X(\boldsymbol{x})$ and $\boldsymbol{k}$ is the wavenumber vector. In the present DNS, we use for the x_1 direction the one-dimensional Gaussian filter in a discrete form,

$$u_i^{[\sigma]_{1D}}(x_1, x_2, x_3, t) = \frac{\sum_{x_1'} u_i(x_1', x_2, x_3, t) \exp\left(\dfrac{-(x_1 - x_1')^2}{2\sigma^2}\right) \Delta}{\sum_{x_1'} \exp\left(\dfrac{-(x_1 - x_1')^2}{2\sigma^2}\right) \Delta}, \tag{2.7}$$

and the Fourier representation (2.6) for the other (i.e. x_2 and x_3) periodic directions to implement the three-dimensional Gaussian filter (2.5). In (2.7) we take the summation for x_1' over the whole domain; that is, the filter length is L_x.

Next, we take the difference between the filtered velocities with two different filter widths σ and 2σ,

$$u_i{}^{(\sigma)}(\boldsymbol{x}, t) = u_i^{[\sigma]}(\boldsymbol{x}, t) - u_i^{[2\sigma]}(\boldsymbol{x}, t), \tag{2.8}$$

which corresponds to a band-pass filter, since it contains information only in the band $[\sigma, 2\sigma)$ of length scales. Hereafter, the superscript $\cdot^{(\sigma)}$ denotes the filter band of $[\sigma, 2\sigma)$.

In the following analyses we first compute $u_i^{(\sigma)}(\boldsymbol{x}, t)$, and then evaluate scale-decomposed quantities, which are simply called quantities at scale σ, from $u_i^{(\sigma)}(\boldsymbol{x}, t)$. For example, we define the second invariant,

$$Q^{(\sigma)} = -\tfrac{1}{2} D_{ij}^{(\sigma)} D_{ji}^{(\sigma)} = \tfrac{1}{2}\left(W_{ij}^{(\sigma)} W_{ij}^{(\sigma)} - S_{ij}^{(\sigma)} S_{ij}^{(\sigma)}\right), \tag{2.9}$$

at scale σ of the scale-decomposed velocity gradient tensor,

$$D_{ij}^{(\sigma)} = \frac{\partial u_i^{(\sigma)}}{\partial x_j} = S_{ij}^{(\sigma)} + W_{ij}^{(\sigma)}. \tag{2.10}$$

Here, $W_{ij} = (D_{ij} - D_{ji})/2$ and $S_{ij} = (D_{ij} + D_{ji})/2$.

Recall that the present system has a mean flow. It is therefore important, in some cases, to consider the scale decomposition of the fluctuation velocity $u_i'(= u_i - \overline{u_i})$ obtained by using the Reynolds decomposition. The band-passed fluctuation velocity $u_i'^{(\sigma)}(\boldsymbol{x}, t)$ is estimated by the difference between $u_i'^{[\sigma]}$ and $u_i'^{[2\sigma]}$ that are defined similarly to $u_i^{[\sigma]}$ and $u_i^{[2\sigma]}$, respectively. Accordingly, we also define $Q'^{(\sigma)}$ by using $u_i'^{(\sigma)}$.

3. Hierarchy of coherent vortices

In this section we demonstrate that the scale decomposition, which is introduced above, captures the hierarchy of coherent vortices. First, we visualize vortices at different scales (figure 3*b–d*) by using the isosurface of $Q'^{(\sigma)}$. Here, we choose thresholds in terms of

https://doi.org/10.1017/jfm.2023.824 Published online by Cambridge University Press

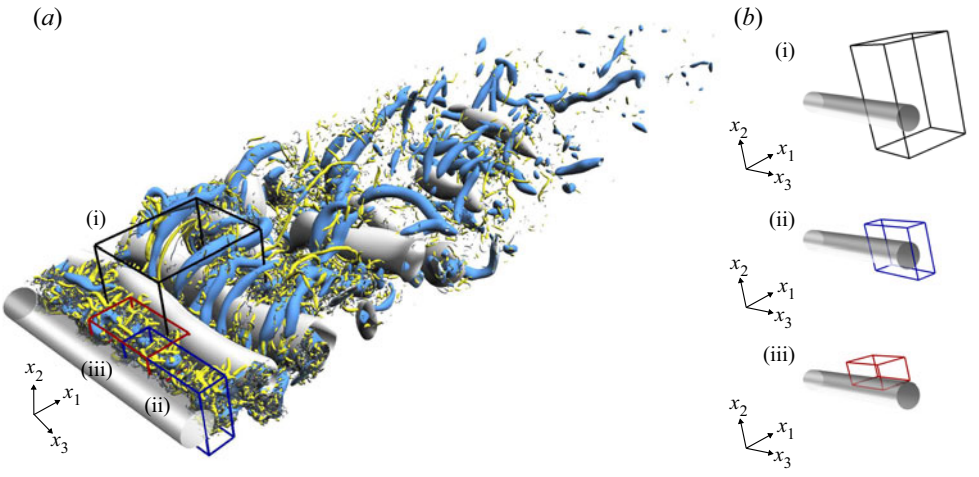

Figure 4. Simultaneous plot of the vortices with different scales in figure 3(*a–d*). The subdomains (i)–(iii) indicate the three distinct regions examined in §§ 3 and 4. See supplementary movie 1 available at https://doi.org/10.1017/jfm.2023.824.

root-mean-square values at $(x_1, x_2) = (3, 0)$ so that we can identify coherent vortices in the three subdomains examined below. We set the filter scales as (*b*) $\sigma = \sigma_{max}$, (*c*) $\sigma_{max}/4$ and (*d*) $\sigma_{max}/16$. Here, we define the largest length scale $\sigma_{\max}$ by $D/(2\pi St)$ (Yasuda, Goto & Vassilicos 2020) with $St = 0.20$ (see § 2.2), which corresponds to the diameter ($\sigma_{max} = 0.8D$) of the shed roller vortices. On the other hand, the smallest scale $\sigma = \sigma_{max}/16$ corresponds to $\sigma = 6.4\Delta$, which means that the three filter scales are well resolved by the DNS grid width. The scale ratio, four, was also used in our previous studies (Goto *et al.* 2017; Motoori & Goto 2019, 2021) because we can identify distinct coherent vortices with this scale ratio. Incidentally, this is consistent with the observation that small vortices are most likely to be perpendicular to four times larger ones (see figure 14 in § 4.4). Figure 3(*b*) for $\sigma = \sigma_{max}$ shows that roller vortices are coherent even in high-Reynolds-number turbulence, though they cannot be observed without the scale decomposition (figure 3*a*). Figures 3(*c*) and 3(*d*) show that smaller vortices, which are larger than the Kolmogorov-scale eddies (figure 3*a*), are also coherent.

Figure 4 simultaneously shows the vortices at four length scales shown in figure 3(*a–d*). We see that these vortices show clear coherence; namely, blue rib vortices are located between grey roller vortices and the axis of ribs is perpendicular to rollers; similarly, further smaller yellow vortices are located around blue rib vortices and the axes of these small vortices tend to be perpendicular to rib vortices. As will be shown in the following sections, these tendencies are due to the creation mechanism that smaller-scale vortices are amplified by being stretched around larger-scale ones. The supplementary movies 1–4 visualize the detailed dynamics.

We also emphasize that, although some smaller vortices exist within a larger vortex, they do not cluster to form the vortex; in other words, even if we lower the threshold of the isosurface for smaller-scale vortices, the isosurface gets connected but they do not form a larger vortex. These observations are similar to turbulence in a periodic cube (Goto 2008; Goto *et al.* 2017), turbulent boundary layers (Motoori & Goto 2019, 2020) and turbulent channel flow (Motoori & Goto 2021). However, the turbulent wake is more complex than these flows because the largest-scale vortices are different depending on regions. To clarify this feature, we examine in the following subsections the sustaining

https://doi.org/10.1017/jfm.2023.824 Published online by Cambridge University Press

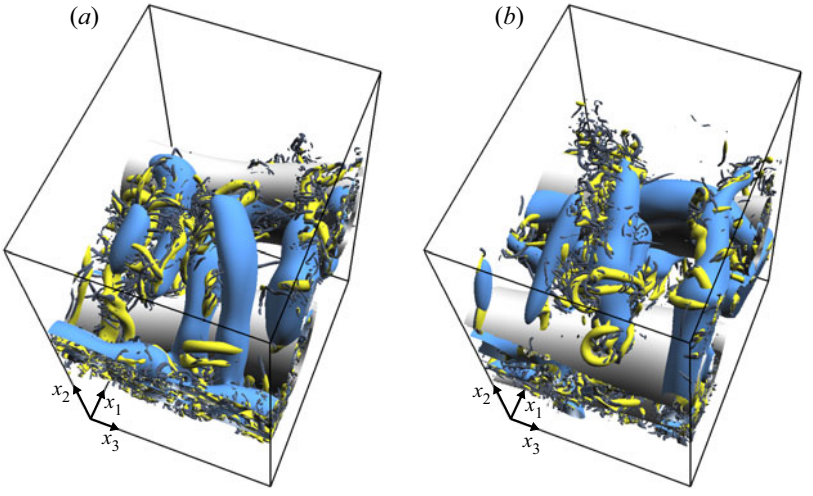

Figure 5. Lagrangian tracking (with the velocity $0.82\overline{u_1}$ at $(x_1, x_2) = (5, 0.6)$) of subdomain (i) that is framed with black lines in figure 4. The subdomain is located in (*a*) $1.2 \leqslant x_1 \leqslant 4.6$ at $t = 0$ and in (*b*) $3.4 \leqslant x_1 \leqslant 6.8$ at $t = 2.4$. See supplementary movie 2.

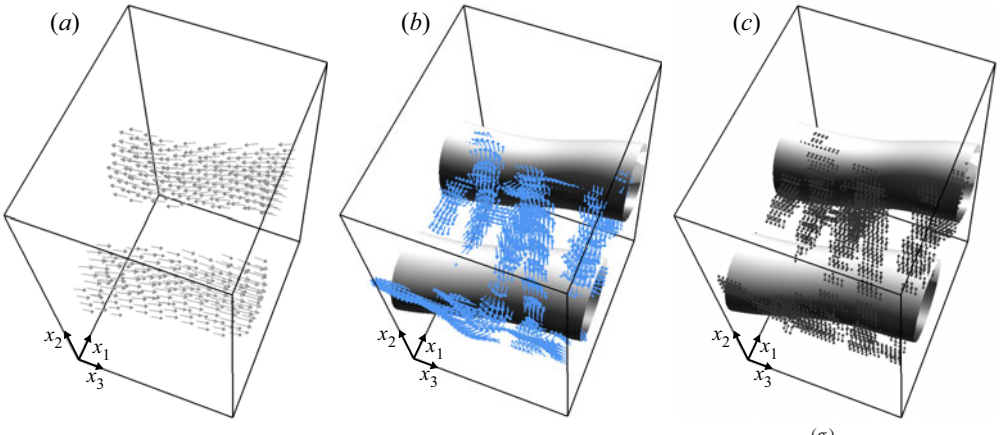

Figure 6. Vorticity direction at (*a*) $\sigma = \sigma_{max}$ and (*b*) $\sigma_{max}/4$. (*c*) Stretching direction $\boldsymbol{e}_1^{(\sigma)}$ at $\sigma = \sigma_{max}$. We show the arrows only in vortices at scales (*a*) $\sigma = \sigma_{max}$ and (*b*,*c*) $\sigma_{max}/4$ shown in figure 5(*a*).

mechanism of the hierarchy of vortices in three distinct regions: (i) the downstream region, (ii) the recirculation region just behind the cylinder and (iii) the separated shear layer. We show the magnified visualizations in each region (i.e. the regions labelled by (i)–(iii) in figure 4) in figures 5–8, respectively.

Incidentally, in figures 3 and 4 we identify coherent vortices by using $Q'^{(\sigma)}$, which is estimated with the Reynolds decomposition. Appendix B shows that $Q^{(\sigma)}$, without the Reynolds decomposition, differs from $Q'^{(\sigma)}$ for larger scales because $Q^{(\sigma)}$ can capture not only these vortices identified by $Q'^{(\sigma)}$ but also a pair of quasi-stationary vortices just behind the cylinder. As will be discussed in § 4.2, these quasi-stationary vortices play crucial roles in the recirculation region. However, in this section we use $Q'^{(\sigma)}$ to identify vortices since the pair of large vortices identified by $Q^{(\sigma)}$ prevent us from observing small vortices near the cylinder.

https://doi.org/10.1017/jfm.2023.824 Published online by Cambridge University Press

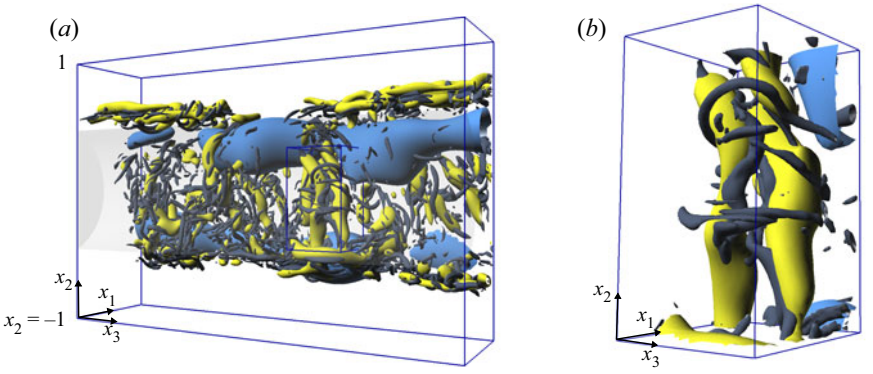

Figure 7. (*a*) Magnification of subdomain (ii) that is framed with blue lines in figure 4. (*b*) Further magnification of the subdomain that is framed with blue lines in (*a*). See supplementary movie 3.

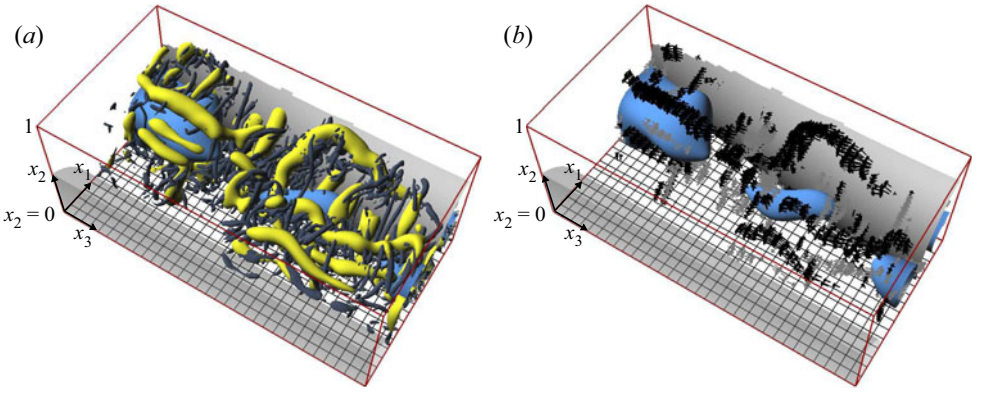

Figure 8. (*a*) Magnification of subdomain (iii) that is framed with red lines in figure 4. The width of the black grid indicates 20η at $(x_1, x_2) = (0.8, 0.5)$. In (*b*) we show the vorticity direction of yellow vortices. Black arrows indicate negative vorticity in the spanwise component (same as the vorticity of the shear layer), whereas grey arrows indicate the positive one. See supplementary movie 4.

3.1. *Downstream region of the wake*

First, we examine the downstream region of the wake where roller vortices exist; see figure 5(*a*), which corresponds to the subdomain labelled by (i) in figure 4. To see the temporal evolution of coherent vortices in this subdomain, we track the subdomain with $0.9U_\infty$ so that a pair of grey rollers remain in the frame. The subdomain is located in $1.2 \leqslant x_1 \leqslant 4.6$ (figure 5*a*) at $t = 0$, and it is in $3.4 \leqslant x_1 \leqslant 6.8$ (figure 5*b*) at $t = 2.4$. We observe in figure 5(*a*) that blue rib vortices tend to align to the stretching direction around the grey pairs of roller vortices. Figure 6 shows the direction of the vorticity $\boldsymbol{\omega}^{(\sigma)}$ of (*a*) roller and (*b*) rib vortices, and figure 6(*c*) shows the eigenvector $\boldsymbol{e}_1'^{(\sigma)}$ corresponding to the maximum eigenvalue of $S_{ij}'^{(\sigma)}$. We can see that the axes of rib vortices are indeed aligned to the stretching direction induced by the roller vortices. This implies that the rib vortices are amplified by vortex stretching, which will be quantitatively verified in the next section. Similar events were also observed in experiments (Lin, Vorobieff & Rockwell 1996) of the turbulent wake at $Re_D = 10^4$. In the downstream region (figure 5*b*) blue rib vortices also tend to form counter-rotating pairs (see also figure 6*b*), while the roller vortices are weakened (see also figure 4), and further smaller vortices (yellow ones) are stretched

https://doi.org/10.1017/jfm.2023.824 Published online by Cambridge University Press

and amplified in the straining regions around these blue vortex pairs. In fact, yellow vortices tend to perpendicularly align to blue ones, i.e. the stretching direction around counter-rotating pairs of rib vortices. Thus, the scale-by-scale cascading events originating from the shed roller vortices are evident in this downstream region. Supplemental movie 2 is also available online to observe these events.

The above observation may imply that the origin of the $-5/3$ power law of the power spectrum (figure 2) in the downstream of the wake is similar to that in homogeneous turbulence. Since vortex-stretching events at different scales simultaneously occur in statistically steady turbulence, vortices at various ages coexist. This makes the observation of each elementary process obscure in turbulence in a periodic cube. In contrast, in a turbulent wake, since smaller-scale vortices are created successively as the flow develops downstream, the elementary process of the cascade is rather clear (figure 5 and movie 2). It is also important that, since the successive cascading events occur outwardly toward the turbulent/non-turbulent interface, Kolmogorov-scale vortices are dominant at the interface. This explains observation (Watanabe *et al.* 2014; Silva, Zecchetto & Da Silva 2018; Watanabe, Da Silva & Nagata 2019) that the interface is accompanied by a sharp change of the vorticity.

3.2. *Recirculation region*

Next, we examine the recirculation region (i.e. $-0.5 \lesssim x_2 \lesssim 0.5$) just behind the cylinder. Recall that the power spectrum $E_2(f)$ obeys the $-5/3$ power law even in this region (figure 2).

In figure 7(a), which is a magnification of subdomain (ii) of figure 4, we visualize the isosurface of Q' (black objects) and $Q'^{(\sigma)}$ with $\sigma = \sigma_{max}/4$ (blue) and $\sigma_{max}/16$ (yellow) in the same region. In this region blue vortices with $\sigma_{max}/4$ are quasi-stationary, which are shedding as roller vortices with σ_{max} in the downstream. It is evident in figure 7(a) and its supplementary movie 3 that smaller yellow vortices tend to align in the x_2 direction, that is, the stretching direction in the velocity field induced by the quasi-stationary blue vortices. This implies that the yellow vortices are stretched and amplified by them.

In figure 7(b) we further magnify a subdomain of figure 7(a). Further smaller (i.e. the Kolmogorov-scale) black vortices tend to be perpendicular to yellow ones. This implies that these vortices are also amplified by the vortex stretching. Incidentally, since the size of yellow vortices is 10–20η, some yellow vortices are identical to black ones.

These observations in figure 7 are, again, similar to turbulence in a periodic cube except that the origin of the cascading events is the blue paired vortices in the wake instead of the largest vortices sustained by some external force in periodic turbulence. In other words, flow in the recirculation region is statistically stationary turbulence, which explains the immediate appearance of the $-5/3$ power law just behind a cylinder. More concretely, the quasi-stationary counter-rotating roller vortices are the source of the energy cascade to create the spectrum. This is consistent with the results obtained by the analysis of the KHMH equation; for example, Alves Portela *et al.* (2020) demonstrated the coherent roller vortices feed energy to stochastic motions, at smaller scales, in turbulence just behind the square prism ($x_1 = 2$). Incidentally, although Yasuda *et al.* (2020) suggested the possibility that the interaction between the shed roller vortices and the smaller-scale vortices in the shear layers (see the next subsection) led to the establishment of the $-5/3$ power-law spectrum, the present visualizations (figure 7) suggest a simpler process of the small-scale vortex generations.

https://doi.org/10.1017/jfm.2023.824 Published online by Cambridge University Press

3.3. *Separated shear layer*

Next, we examine the region ($0.2 \leqslant x_1 \leqslant 1.5$, $0 \leqslant x_2 \leqslant 1$) around one of the shear layers attached to the cylinder; see figure 8, which is a subdomain labelled by (iii) in figure 4. The transparent object in the figure is the cylinder. Figure 8(*a*) shows that upstream yellow vortices are parallel to the cylinder. We also show in figure 8(*b*) the rotational direction of these vortices identified by the vorticity. The black arrows show the same vorticity direction as the mean shear layer, while the grey ones show the opposite. We can see that these yellow vortices tend to form counter-rotating pairs. There also exist smaller black vortices, whose diameter is approximately 10η, around these yellow vortices. Note that the grid width drawn on the bottom of the subdomain is 20η at $(x_1, x_2) = (0.8, 0.5)$. The events of the amplification of smaller vortices are more evident in supplementary movie 4. The observation suggests that the yellow shear layer vortices are parents and they stretch and amplify smaller ones.

For $Re_D \gtrsim 6000$, vortices are deformed in the shear layer to interact with the shed vortices in the recirculation region (Norberg 2003). In such a case, although these parent vortices in the two regions can interact, the generation mechanism of sufficiently smaller vortices may not be altered; that is, they are generated through the successive vortex stretching. In fact, Aasland *et al.* (2022) demonstrated that smaller-scale streamwise vortices are generated by being stretched by the shear layer vortices even for $Re_D = 10^4$.

3.4. *Summary of observations*

We have unraveled the generation mechanism of the hierarchies of coherent vortices in three distinct regions. In all of the regions, smaller vortices are generated by vortex stretching due to about four times (recall that the scale ratio between the successive filter scales is four in figures 3–8) larger vortices, but the origin of the cascading process is different in these three regions: (i) the shed roller vortices in the downstream of the wake, (ii) the counter-rotating pair of the quasi-stationary vortices in the recirculation region, and (iii) the shear layer vortices in the shear layer.

Since the three regions overlap, around their boundaries, we observe different generation mechanisms of vortices. For example, in figure 7 (i.e. recirculation region) yellow vortices in the bulk are stretched by quasi-stationary pairs (around $x_2 \approx 0$), while we also observe those are parallel to the cylinder in the shear layer (around $x_2 \approx \pm 0.5$). In figure 8 (i.e. the separated shear layer), while the upstream yellow vortices are generated in the shear layer, we also observe the downstream vortices aligned in the streamwise direction, which are stretched by quasi-stationary vortices and/or shed rollers.

In addition, in figure 4 we can see some of downstream yellow vortices ($\sigma = \sigma_{max}/16$) stretched by grey roller vortices ($\sigma = \sigma_{max}$). This is because, as will be shown quantitatively in the next section, the vortex stretching contributes to a wide range of scales, though the contribution is strongest with the scale ratio being about four.

Before closing this section, it is worth mentioning that many authors recently described the energy cascade in terms of different mechanisms: for example, the reconnection of anti-parallel vortices (Yao & Hussain 2022; Yao, Mollicone & Papadakis 2022) and the elliptical instability due to interactions between vortices (McKeown *et al.* 2018; Mckeown *et al.* 2020). It was also reported that strain-rate self-amplification plays a crucial role in energy transfer (Carbone & Bragg 2020; Johnson 2021). Although the other mechanisms can contribute to the energy transfer, in the following analyses we quantify the energy transfer due to the vortex stretching to verify that the events shown in the present section contribute to the transfer.

https://doi.org/10.1017/jfm.2023.824 Published online by Cambridge University Press

4. Scale-dependent energy transfer due to vortex stretching

To quantify the energy cascading events observed in the previous section, we define the energy transfer rates due to the vortex stretching as

$$\overline{\mathcal{T}'}(\sigma_S \to \sigma_\omega) = \overline{(\omega_i'^{(\sigma_\omega)} S_{ij}'^{(\sigma_S)} \omega_j'^{(\sigma_\omega)})}\sigma_\omega^2. \tag{4.1}$$

Here, $\bar{\cdot}$ denotes the average over x_3 and t. Since $\omega_i'^{(\sigma_\omega)}$ is the vorticity evaluated from $u_i'^{(\sigma_\omega)}$ and since $S_{ij}'^{(\sigma_S)}$ is the strain-rate tensor evaluated from $u_i'^{(\sigma_S)}$, the quantity $\omega_i'^{(\sigma_\omega)} S_{ij}'^{(\sigma_S)} \omega_j'^{(\sigma_\omega)}$ in (4.1) indicates the contribution to the stretching of vorticity at σ_ω from strain-rate fields at σ_S on average. Here, we have assumed that the off-diagonal terms $\omega_i'^{(\sigma_\omega')} S_{ij}'^{(\sigma_S)} \omega_j'^{(\sigma_\omega)}$ with $\sigma_\omega' \neq \sigma_\omega$ and the advection term have smaller contributions to the enstrophy production rate. The former assumption may be justified by the observation that vortices at different scales are located in distinct regions (Yoneda *et al.* 2022). Although the amplification of enstrophy due to vorticity advection seems weaker in three-dimensional turbulence, quantitative evidence is needed to justify the latter assumption. We have also assumed that the viscous effect is negligible in the inertial range ($\sigma_\omega \gg \eta$). This scale-dependent enstrophy production rate $\overline{\omega_i'^{(\sigma_\omega)} S_{ij}'^{(\sigma_S)} \omega_j'^{(\sigma_\omega)}}$ due to vortex stretching was also used to investigate the generation mechanism of the hierarchy of vortices in periodic turbulence (Goto *et al.* 2017), turbulent boundary layers (Motoori & Goto 2019) and turbulent channel flow (Motoori & Goto 2021). In the present study we multiply the enstrophy production rate by σ_ω^2 to quantify the production rate of the energy at σ_ω. Therefore, $\overline{\mathcal{T}'}$ indicates the interscale energy transfer rate due to vortex stretching. When $\overline{\mathcal{T}'}(\sigma_S \to \sigma_\omega)$ is positive, the energy of vortices at σ_ω is amplified due to vortex stretching by strain rate at σ_S on average; otherwise, the energy contained by vortices at σ_ω is weakened due to the vortex compression by vortices at σ_S. The definition of the energy transfer (4.1) is similar to the quantity defined by Yoneda *et al.* (2022) for homogeneous isotropic turbulence.

Note that the mean strain rate $\overline{S_{ij}}$ can also contribute to the enstrophy production in addition to (4.1). To quantify this contribution, we define

$$\overline{\mathcal{T}_M}\,(M \to \sigma_\omega) = \overline{(\omega_i'^{(\sigma_\omega)} \overline{S_{ij}} \omega_j'^{(\sigma_\omega)})}\sigma_\omega^2. \tag{4.2}$$

Note that, since x_3 direction is homogeneous ($\overline{S_{13}} = \overline{S_{31}} = \overline{S_{23}} = \overline{S_{32}} = \overline{S_{33}} = 0$), only the components of $\overline{S_{12}}(= \overline{S_{21}})$ and $\overline{S_{22}}(= -\overline{S_{11}})$ are non-zero. Figure 9 shows the distribution of (*a*) $\overline{S_{12}}$ and (*b*) $\overline{S_{22}}$. In the downstream along the centreline ($x_2 \approx 0$), the mean strain rates are small; whereas, around $x_2 \approx \pm 0.5$, the mean shear $|\overline{S_{12}}|$ can be as large as $O(1)$. Hence, in the free shear layer in the downstream regions (i) and separated shear layer (iii), $\overline{\mathcal{T}_M}$ indicates the contribution to the energy transfer from the mean shear $\overline{S_{12}}$.

In the recirculation region (ii) we do not use the Reynolds decomposition. This is because $\overline{\mathcal{T}_M}$ in this region does not quantify the contribution from the mean shear $\overline{S_{12}}$ but from the quasi-stationary vortices behind the cylinder. We therefore evaluate

$$\bar{\mathcal{T}}\,(\sigma_S \to \sigma_\omega) = \overline{(\omega_i^{(\sigma_\omega)} S_{ij}^{(\sigma_S)} \omega_j^{(\sigma_\omega)})}\sigma_\omega^2 \tag{4.3}$$

in the recirculation region (ii) instead of $\overline{\mathcal{T}'}$ and $\overline{\mathcal{T}_M}$. Here, $\omega_i^{(\sigma_\omega)}$ is the vorticity evaluated from the total velocity $u_i^{(\sigma_\omega)}$ at σ_ω without the Reynolds decomposition and $S_{ij}^{(\sigma_S)}$ is the strain-rate tensor evaluated from $u_i^{(\sigma_S)}$. See Appendix B for the visualizations without the Reynolds decomposition.

https://doi.org/10.1017/jfm.2023.824 Published online by Cambridge University Press

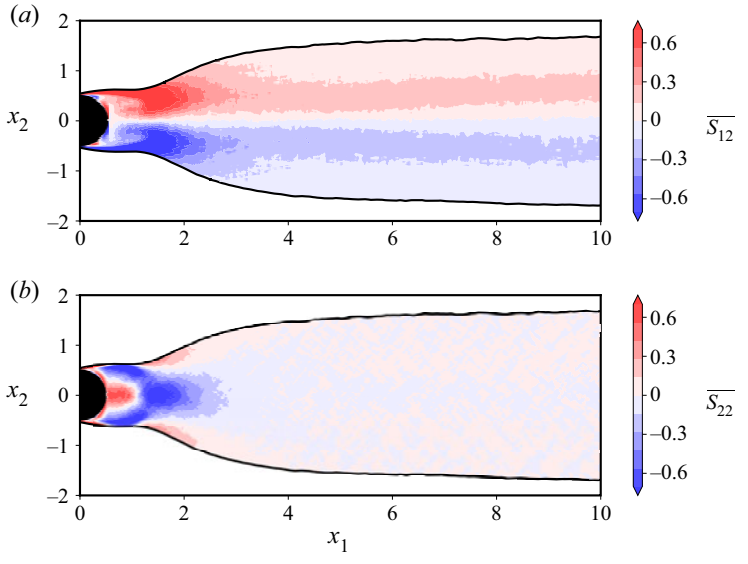

Figure 9. Mean strain-rate fields (*a*) $\overline{S_{12}}$ and (*b*) $\overline{S_{22}}$. Only the region with $\overline{u_1} < 1$ is shown.

In the following subsections, to quantify the energy transfer in the events observed in figures 4–8, we evaluate $\overline{T'}$, $\overline{T_M}$ and $\bar{T}$ under the condition of $Q'^{(\sigma_\omega)} > 0$ (or $Q^{(\sigma_\omega)} > 0$). We examine six scales (σ_{max}, $\sigma_{max}/2$, $\sigma_{max}/4$, $\sigma_{max}/8$, $\sigma_{max}/16$ and $\sigma_{max}/32$) at several positions in the downstream region (§ 4.1), the recirculation region (§ 4.2) and the separated shear layer (§ 4.3).

4.1. *Downstream region of the wake*

We show, in figure 10(*a*), $\overline{T'}$ (grey) at the location $(x_1, x_2) = (3, 0)$, which is on the centreline in the downstream region (figure 5*a*). Note that the vertical axis denotes $\overline{T'}$ normalized by the mean energy dissipation rate $\bar{\epsilon}$ and the horizontal one denotes σ_S/σ_ω. Looking at the black open squares ($\sigma_\omega = \sigma_{max}/32$), we see that the twice-larger-scale ($\sigma_S/\sigma_\omega = 2$) strain-rate fields contribute most to the energy transfer due to vortex stretching. We also see that the four times larger-scale ($\sigma_S/\sigma_\omega = 4$) strain rates contribute secondly. These trends are also the case for the smaller scales $\sigma_\omega = \sigma_{max}/16$ (closed squares), $\sigma_{max}/8$ (open triangles) and $\sigma_{max}/4$ (closed triangles). Therefore, vortices smaller than the roller vortices ($\sigma_\omega \ll \sigma_{max}$) are stretched in the twice and four times larger-scale strain-rate fields, and through this process, they receive the energy. This is consistent with the visualizations (figure 5); namely, blue rib vortices with size $\sigma_{max}/4$ are stretched by the roller vortices, and further smaller vortices (yellow ones with size $\sigma_{max}/16$) are amplified by rib vortices.

It is also important that $\overline{T'}(\sigma_S \to \sigma_\omega)$ for $\sigma_\omega \leqslant \sigma_{max}/8$ collapse. This implies that, through a few steps of the scale-by-scale vortex stretching, small-scale statistics attain self-similarity. This observation is similar to that in turbulence in a periodic cube (Yoneda *et al.* 2022).

In addition, figure 10(*a*) shows that $\overline{T'}$ is negative for $\sigma_S < \sigma_\omega$. This implies that smaller vortices, which are created by being stretched around larger vortices, are likely to compress their parent vortices on average. The vortex compression by smaller vortices is also consistent with the observations in figure 5 and movie 2; for example, pairs of

https://doi.org/10.1017/jfm.2023.824 Published online by Cambridge University Press

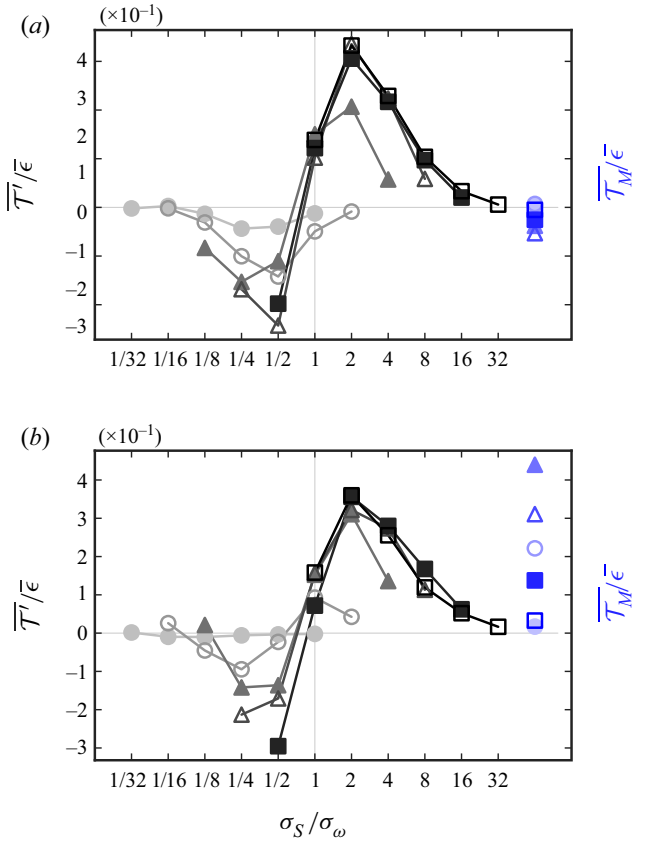

Figure 10. Average energy transfer rate $\overline{\mathcal{T}'}$ due to the vortex stretching by fluctuation strain rates at scale σ_S to fluctuation vorticity at $\sigma_\omega = \sigma_{max}/32$ (open squares), $\sigma_{max}/16$ (closed squares), $\sigma_{max}/8$ (open triangles), $\sigma_{max}/4$ (closed triangles), $\sigma_{max}/2$ (open circles) and σ_{max} (closed circles) at locations (*a*) $(x_1, x_2) = (3, 0)$ and (*b*) $(3, 0.6)$. Blue symbols indicate the transfer rate $\overline{\mathcal{T}_M}$ from the mean strain rates.

rib vortices induce strong straining fields, where smaller vortices are generated; whereas they also induce compressing fields on the other side of the pairs, where their parent (roller) vortices are weakened. Note that the vortex compression by smaller vortices implies the forward energy cascade. It is also important to see that, for small scales $\sigma_\omega (\leqslant \sigma_{max}/8)$, the total energy transfer from larger scales ($\sigma_S > \sigma_\omega$) due to vortex stretching is approximately balanced with the negative transfer from small scales ($\sigma_S < \sigma_\omega$) due to the vortex compression; more precisely, although there is imbalance because of the viscous effect for the present Re_D, the energy transfer caused by vortex stretching and compression is balanced in the inertial range for higher Reynolds numbers (see figure 1(*b*) in Yoneda *et al.* 2022). We will develop further arguments on this point in § 5.

Next, we see, in figure 10(*b*), $\overline{\mathcal{T}'}$ and $\overline{\mathcal{T}_M}$ at $(x_1, x_2) = (3, 0.6)$ in the free shear layer in the downstream region. Similarly to the downstream core region (figure 10*a*), vortices at the small scales $\sigma_\omega \leqslant \sigma_{max}/8$ receive the energy by being stretched by twice and four times larger-scale strain rates. The difference is in $\overline{\mathcal{T}_M}$; more concretely, $\overline{\mathcal{T}_M}$ for vortices at $\sigma_\omega = \sigma_{max}/4$ (closed triangles) is the largest among the six scales and this value is comparable to $\overline{\mathcal{T}'}(2\sigma_\omega \to \sigma_\omega)$. This means that rib vortices, which are stretched between counter-rotating pairs of the roller vortices in the core region, are also stretched by the mean shear around

https://doi.org/10.1017/jfm.2023.824 Published online by Cambridge University Press

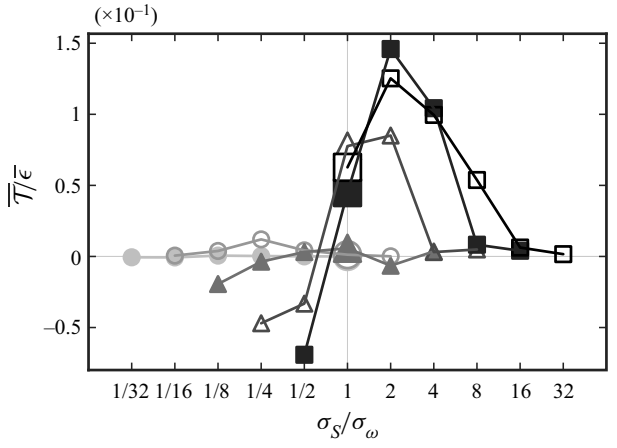

Figure 11. Average energy transfer rate $\bar{\mathcal{T}}$ due to the vortex stretching by total strain rates at scale σ_S to fluctuation vorticity at $\sigma_\omega = \sigma_{max}/32$ (open squares), $\sigma_{max}/16$ (closed squares), $\sigma_{max}/8$ (open triangles), $\sigma_{max}/4$ (closed triangles), $\sigma_{max}/2$ (open circles) and σ_{max} (closed circles) at location $(x_1, x_2) = (0.65, 0)$.

$x_2 = \pm 0.6$. We emphasize that, however, rib vortices are initially stretched around $x_2 \approx 0$ by the roller vortices (see movie 2).

4.2. *Recirculation region*

Next, we turn to the recirculation region (figure 7). Here, we evaluate $\mathcal{T}$ defined as (4.3), which contains the contribution from the quasi-stationary vortices. Figure 11 shows $\bar{\mathcal{T}}$ at $(x_1, x_2) = (0.65, 0)$. Looking at the black open squares ($\sigma_\omega = \sigma_{max}/32$), we can see that the twice-larger-scale strain-rate fields contribute most to the energy transfer, and the four times larger-scale ones are next. These are also the case for $\sigma_\omega = \sigma_{max}/16$ (closed squares). These results are consistent with the events shown in figure 7 and supplementary movie 3; namely, yellow vortices with size $\sigma_{max}/16$ are stretched by the counter-rotating quasi-stationary vortices and further smaller black vortices are stretched by yellow ones.

Here, we emphasize that the cascading events occur locally in the recirculation region. We show in figure 12 the ratio of the advection time scale $T_A = D/U$ ($U = \sqrt{\overline{u_i}^2}$) to the cascading time scale $T_C = 1/S$ ($S = \sqrt{\overline{S_{ij}}^2}$). In the darker colour region with $T_A/T_C > 1$, which is surrounded by the blue line ($T_A/T_C = 1$), the cascade is faster than the advection. The spatial locality of the energy cascade explains that the $-5/3$ power law, which was also observed in other wakes (e.g. Gomes-Fernandes *et al.* 2015; Alves Portela *et al.* 2017, 2020), is established immediately behind an obstacle. In contrast, in a downstream region ($x_1 \gtrsim 2$), advection is faster than the cascade. This is the reason why we have tracked in § 3.1 vortices with the advection velocity.

4.3. *Separated shear layer*

Figure 13 shows $\overline{\mathcal{T}'}$ (grey) and $\overline{\mathcal{T}_M}$ (blue) at $(x_1, x_2) = (0.8, 0.65)$ in the separated shear layer (figure 8). Similarly to the downstream and recirculation regions, to $\overline{\mathcal{T}'}$ for small vortices (the open squares, $\sigma_\omega = \sigma_{max}/32$), the contribution from the twice-larger-scale strain-rate fields is most significant. This verifies the observation (figure 8 and movie 4) that the shear layer vortices stretch and amplify black smaller vortices. However, it

https://doi.org/10.1017/jfm.2023.824 Published online by Cambridge University Press

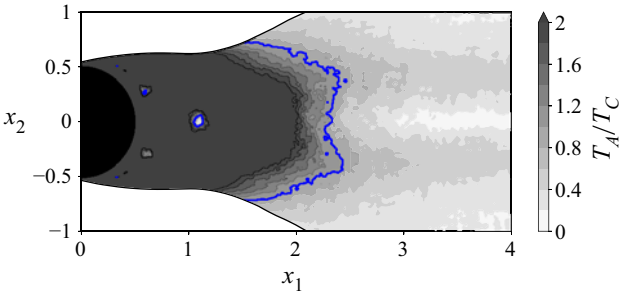

Figure 12. Ratio between the cascading time (T_c) and the advection time (T_A) by the mean flow in the recirculation region. The blue line indicates $T_A/T_C = 1$.

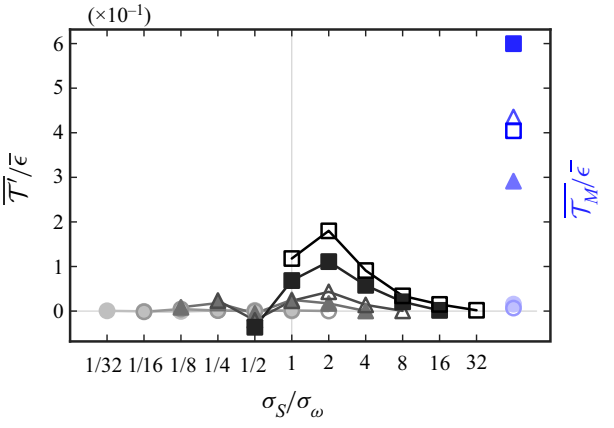

Figure 13. Same as in figure 10 but the results for $(x_1, x_2) = (0.8, 0.65)$.

is evident that the transfer $\overline{\mathcal{T}_M}$ from the mean flow is also significant even for the smallest-scale ($\sigma_{max}/32$) vortices. This is because $\sigma_\omega = \sigma_{max}/32 \approx 7.6\eta$ is comparable with the Corrsin length scale $L_c = \bar{\epsilon}^{1/2}\overline{S_{12}}^{-3/2}$ ($\sigma_\omega = 0.24L_c$). Motoori & Goto (2019) showed that vortices larger than L_c are stretched mainly by the mean shear in turbulent boundary layers, and this is also the case in the separated shear layer. Incidentally, if the Reynolds number is higher, further smaller-scale ($\sigma_\omega \ll L_c$) vortices can be created by twice-larger-scale vortices.

4.4. *Alignment between stretching direction and vorticity*

In §§ 4.1–4.3 we have demonstrated that smaller vortices are generated by being stretched by larger (more, precisely, twice larger) vortices in all the three regions of the wake. Here, we show that this is consistent with the observation in § 3 that small vortices tend to be aligned in the straining regions induced by four times larger vortices.

To this end, we rewrite the scale-dependent enstrophy production rate in (4.1) as

$$\omega_i'^{(\sigma_\omega)} S_{ij}'^{(\sigma_S)} \omega_j'^{(\sigma_\omega)} = s_i'^{(\sigma_S)} (\boldsymbol{e}_i'^{(\sigma_S)} \cdot \boldsymbol{\omega}'^{(\sigma_\omega)})^2, \tag{4.4}$$

where $s_i'^{(\sigma_S)}$ ($s_1'^{(\sigma_S)} \geqslant s_2'^{(\sigma_S)} \geqslant s_3'^{(\sigma_S)}$) are the eigenvalues of $S_{ij}'^{(\sigma_S)}$ and $\boldsymbol{e}_i'^{(\sigma_S)}$ are the corresponding eigenvectors. Note that $s_1'^{(\sigma_S)} + s_2'^{(\sigma_S)} + s_3'^{(\sigma_S)} = 0$ for incompressible fluids.

https://doi.org/10.1017/jfm.2023.824 Published online by Cambridge University Press

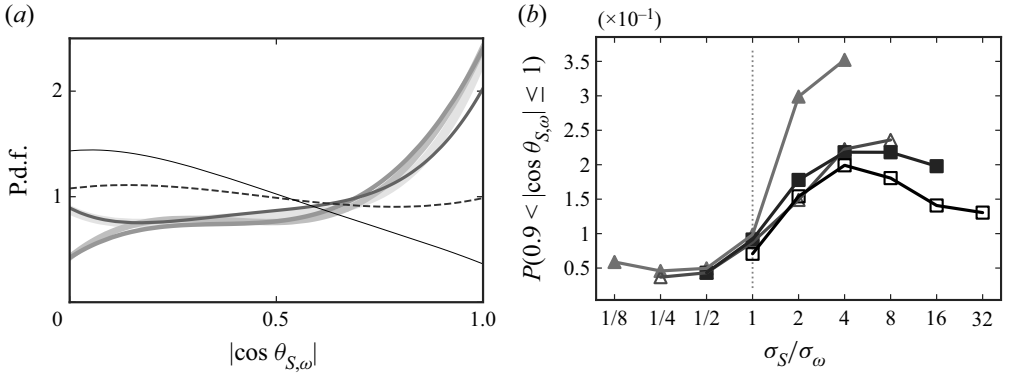

Figure 14. (*a*) The p.d.f. of $|\cos\theta_{S,\omega}|$ for $\sigma_\omega = \sigma_{max}/16$ in the region $Q'^{(\sigma_\omega)} > 0$ at $(x_1, x_2) = (3, 0.6)$. The six lines show, from the thinner (and darker) to thicker (and lighter), $\sigma_S/\sigma_\omega = 0.5$, 1, 2, 4, 8 and 16. The dashed line shows the self-alignment (i.e. $\sigma_S/\sigma_\omega = 1$). (*b*) Probability of $0.9 < |\cos\theta_{S,\omega}| \leqslant 1$ for $\sigma_\omega = \sigma_{max}/32$ (open squares), $\sigma_{max}/16$ (closed squares), $\sigma_{max}/8$ (open triangles) and $\sigma_{max}/4$ (closed triangles).

We here define the alignment between the vorticity and stretching direction as

$$\cos\theta_{S,\omega}(\sigma_S, \sigma_\omega) = \boldsymbol{e}_1'^{(\sigma_S)} \cdot \tilde{\boldsymbol{\omega}}'^{(\sigma_\omega)}, \tag{4.5}$$

where $\tilde{\boldsymbol{\omega}}'^{(\sigma_\omega)}$ is the normalized vorticity $\boldsymbol{\omega}'^{(\sigma_\omega)}/|\omega'^{(\sigma_\omega)}|$. A similar quantity was evaluated in periodic turbulence (Leung *et al.* 2012; Goto *et al.* 2017) and turbulent boundary layers (Motoori & Goto 2019) to show that small-scale vorticity tends to align with the stretching direction at the four times larger scale. Goto *et al.* (2017) also quantitatively showed that smaller vortices tend to be perpendicular to larger ones by using vortex axes identified with the low-pressure method (Miura & Kida 1997; Kida & Miura 1998).

To demonstrate this tendency in the turbulent wake, we plot in figure 14(*a*) the probability density function (p.d.f.) of $|\cos\theta_{S,\omega}|$ for $\sigma_\omega = \sigma_{max}/16$ at $(x_1, x_2) = (3, 0.6)$. The probability P of $|\cos\theta_{S,\omega}| > 0.9$ for $\sigma_S/\sigma_\omega \geqslant 2$ (darker lines) is larger than unity. This implies that smaller-scale vortices tend to align with the stretching direction at larger scales. Then, we show in figure 14(*b*) the probability P of $0.9 < |\cos\theta_{S,\omega}| \leqslant 1$ for vortices at several scales ($\sigma_\omega = \sigma_{max}/4$, $\sigma_{max}/8$, $\sigma_{max}/16$ and $\sigma_{max}/32$). Looking at the results (closed triangles, $\sigma_\omega = \sigma_{max}/4$) for rib vortices, we see that these vortices are most likely to be aligned to the stretching direction at the scale four times as large as themselves. We also see vortices at scale $\sigma_{max}/16$ align most to the stretching direction of rib vortices ($\sigma_{max}/4$). These observations are consistent with those in § 3.1, that is, blue rib vortices are perpendicular to grey rollers; similarly, further smaller yellow vortices tend to be perpendicular to rib vortices. We can also see a similar tendency of the alignment for smaller-scale vortices (other symbols in figure 14*b*) and for other locations. In summary, as observed in the visualizations (figures 5–8) and in the quantification (figure 14), smaller vortices always tend to align perpendicular to four times larger vortices. However, this is not inconsistent with the result that the twice larger vortices contribute most to the energy transfer (figures 10, 11 and 13), since $s_i'^{(\sigma_S)}$ is larger for smaller scales. In other words, as a result of the competition between the magnitude of $s_i'^{(\sigma_S)}$ and the alignment of $\boldsymbol{e}_i'^{(\sigma_S)}$ and $\boldsymbol{\omega}'^{(\sigma_\omega)}$, the strain rate at scales twice as large as the vortices is dominant in the energy transfer due to vortex stretching.

https://doi.org/10.1017/jfm.2023.824 Published online by Cambridge University Press

5. Relevance to the energy cascade

As shown in § 4, vortices are stretched by larger ones and compressed by smaller ones on average. If this vortex stretching process corresponds to the energy cascade, the parent vortices must lose their energy as smaller-scale vortices acquire it. The energy reduction might be due to the vortex compression by smaller vortices, though our previous studies (Goto 2008; Goto *et al.* 2017; Motoori & Goto 2019, 2021; Yoneda *et al.* 2022) did not show clear evidence. Here, to describe the energy cascading process in instantaneous fields in terms of the vortex stretching and compression, we examine the downstream region where the multilevel hierarchy of coherent vortices exists.

First, to examine the energy transfer due to the vortex stretching by four times larger-scale vortices, we define

$$\mathcal{T}_{L\to S} = \left(\omega_i'^{(\sigma/4)} S_{ij}'^{(\sigma)} \omega_j'^{(\sigma/4)}\right) \sigma^2. \tag{5.1}$$

This is the unaveraged quantity in (4.1) with the fixed scale of strain rates as $\sigma_S = 4\sigma_\omega$; recall that vortices tend to align in the straining regions induced by the four times larger vortices (§ 4.4). When $\mathcal{T}_{L\to S}$ is positive, the larger vortices amplify the energy of smaller vortices through the vortex stretching; otherwise, they reduce the energy of smaller ones through the vortex compression.

We plot in figure 15(*a*) the active regions of positive and negative energy transfers due to vortex stretching and compression by the isosurfaces of positive (yellow) and negative (red) $\mathcal{T}_{L\to S}(= \pm 6.4 \times 10^{-3})$ for $\sigma = \sigma_{max}$, respectively. For visibility, we do not display in panel (*b*) the yellow objects. Comparing these panels, we see that yellow isosurfaces coincide with most of the blue rib vortices. We can also see that the red regions are fewer than the yellow ones and they do not correlate with rib vortices. The observations are the direct evidence that rib vortices are created by being stretched by roller vortices.

To show the relevance of the scale-local vortex stretching to the energy cascade, it is necessary to demonstrate that the energy of larger vortices is reduced through the vortex interactions. For this purpose, we define the energy transfer from smaller to larger vortices as

$$\mathcal{T}_{S\to L} = \left(\omega_i'^{(\sigma)} S_{ij}'^{(\sigma/4)} \omega_j'^{(\sigma)}\right) \sigma^2, \tag{5.2}$$

fixing the scale of strain rates to a quarter as large as that of vorticity for the unaveraged quantity in (4.1). When $\mathcal{T}_{S\to L}$ is negative, the energy of larger vortices is reduced by smaller ones through the vortex compression; otherwise, the energy of larger vortices is amplified by smaller ones.

Figure 16 shows the positive (yellow) and negative (red) isosurfaces of $\mathcal{T}_{S\to L}$ for $\sigma = \sigma_{max}$. Both compression (red) and stretching (yellow) regions are alternatively observed along the axis of roller vortices. This observation is quantified in figure 17(*a*) by the p.d.f. of $\mathcal{T}_{S\to L}$ inside the roller vortices at σ_{max} (see the lightest grey line). We can see that the probabilities of both of $\mathcal{T}_{S\to L} > 0$ and $\mathcal{T}_{S\to L} < 0$ are not small. A rib vortex forms a counter-rotating pair with adjacent vortices, and therefore, they stretch and compress the roller vortices as observed in figure 16. However, we emphasize that, on average, the energy of a single roller vortex is reduced by rib vortices. To show this, we evaluate the spatially local average, $\langle \mathcal{T}_{S\to L}\rangle_Q$, of $\mathcal{T}_{S\to L}$ inside each of the individual vortices identified by the isosurface of $Q'^{(\sigma)}$, and we plot in figure 17(*b*) the p.d.f. of $\langle \mathcal{T}_{S\to L}\rangle_Q$. The lightest grey line shows the results for $\sigma = \sigma_{max}$. It is evident that negative values of $\langle \mathcal{T}_{S\to L}\rangle_Q$ are more dominant. This implies that rib vortices tend to compress roller vortices; consequently, roller vortices are weakened in total even in instantaneous fields. This tendency is also observed irrespective of the scale σ of vortices (see the other lines in figure 17*b*).

https://doi.org/10.1017/jfm.2023.824 Published online by Cambridge University Press

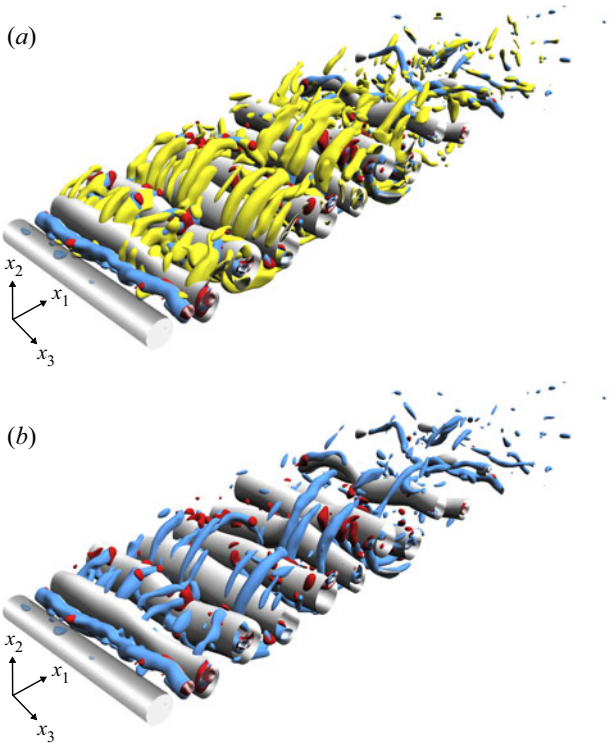

Figure 15. Positive (yellow, shown only in panel *a*) and negative (red) isosurfaces of the energy transfer $\mathcal{T}_{L\to S}$ for $\sigma = \sigma_{max}$ through the vortex stretching and compression, respectively. The thresholds are $\mathcal{T}_{L\to S} = \pm 6.4 \times 10^{-3}$. Grey and blue objects are the isosurfaces of $Q^{\prime(\sigma_{max})}$ and $Q^{\prime(\sigma_{max}/4)}$, respectively. Their thresholds are the same as in figure 3.

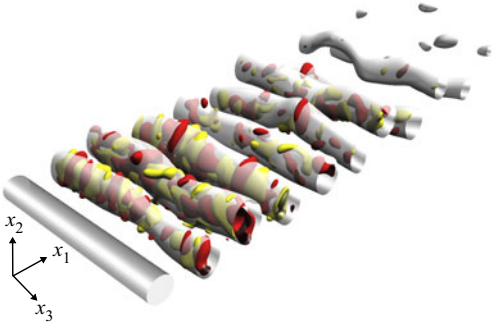

Figure 16. Positive (yellow) and negative (red) isosurfaces of the energy transfer $\mathcal{T}_{S\to L}$ for $\sigma = \sigma_{max}$ through the vortex stretching and compression, respectively. The thresholds are $\mathcal{T}_{L\to S} = \pm 6.3 \times 10^{-3}$. Grey objects are the isosurfaces of $Q^{\prime(\sigma_{max})}$, whose threshold is the same as in figure 3.

We have observed that larger vortices are not only compressed by smaller ones but also stretched. The latter phenomenon is reminiscent of the backscatter of energy. However, the present observation can be different from the backscatter observed in studies by LES or the KHMH equation because we examine the energy transfer due to vortex stretching and compression between two different scales. Nevertheless, since the stretching of larger vortices by smaller ones (yellow regions in figure 16) and the compression of smaller

https://doi.org/10.1017/jfm.2023.824 Published online by Cambridge University Press

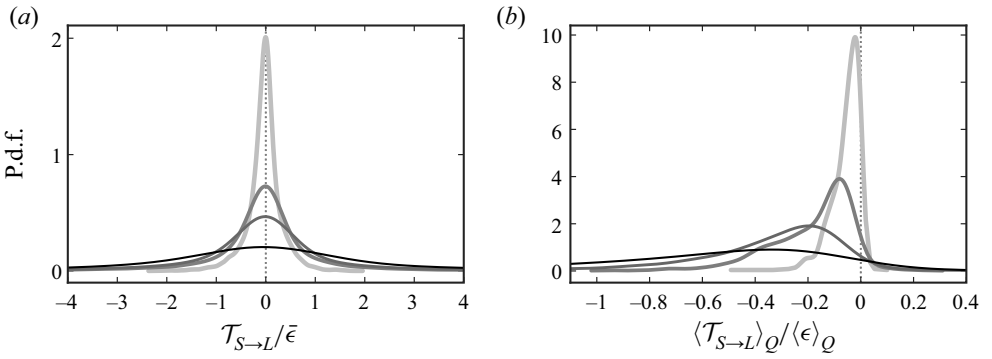

Figure 17. The p.d.f. of (*a*) $\mathcal{T}_{S\to L}/\bar{\epsilon}$ and (*b*) $\langle\mathcal{T}_{S\to L}\rangle_Q/\langle\epsilon\rangle_Q$ for scales $\sigma = \sigma_{max}$ (light grey), $\sigma_{max}/2$ (grey), $\sigma_{max}/4$ (dark grey) and $\sigma_{max}/8$ (black). We normalize the values of the horizontal axis by (*a*) $\bar{\epsilon}$ at $(x_1, x_2) = (3, 0)$ and by (*b*) the energy dissipation rate $\langle\epsilon\rangle_Q$ averaged inside each single vortex. In (*b*) we exclude the results for too small vortices (the volume of the identified vortices is smaller than $(2\sigma)^3$) from the p.d.f.

vortices by larger ones (red regions in figure 15) are physically interpretable, these events may provide clues about the physical mechanism of the backscatter of energy.

6. Conclusions

To investigate the hierarchy of coherent vortices in turbulent wake sustained behind a cylinder, we have conducted DNS of fully developed turbulence for $Re_D = 5000$. By decomposing the obtained velocity fields with the band-pass filter (2.8), we extract vortices at different scales. The isosurfaces of the second invariant of the scale-decomposed velocity gradient tensor capture the three kinds of hierarchies of coherent vortices. To elucidate the generation mechanism of these vortices, we track them (see figures 4–8 and the supplemental movies) in the three distinct regions: (i) the downstream region in the wake, (ii) the recirculation region just behind the cylinder and (iii) the separated shear layers. In all the three regions, the generation mechanism of smaller vortices is common. They are generated in the direction perpendicular to four times larger vortices, being stretched by them (figures 5–8); however, the origin of the cascading process is different in these regions: (i) the shed roller vortices in the downstream region, (ii) a quasi-stationary pair of vortices in the recirculation region, and (iii) the large vortices in the separated shear layers. We have quantitatively verified these observations by evaluating the energy transfers (4.1) or (4.3) due to the vortex stretching (§ 4). More concretely, the twice and four times larger strain-rate fields contribute most to the vortex stretching on average. In conclusion, the generation mechanism of small-scale vortices in turbulence behind a cylinder is similar to that in periodic turbulence (Goto *et al.* 2017), turbulent boundary layers (Motoori & Goto 2019) and turbulent channel flow (Motoori & Goto 2021).

Although counter-rotating smaller vortices, which are created around larger ones, compress and stretch their parent vortices locally in space (figure 16), the total contribution to each parent vortex is dominated by the compression (figure 17*b*). Through this vortex compression of larger vortices by smaller ones, the energy at large scales is reduced and its energy is transferred to small scales due to the stretching of smaller vortices by larger ones. Although we cannot deny the possibility that another mechanism also leads to energy cascade, the present results, in particular the observation of the space-local energy transfer (figures 15–17), may suggest that the vortex stretching/compression processes can explain the energy cascade in turbulence.

https://doi.org/10.1017/jfm.2023.824 Published online by Cambridge University Press

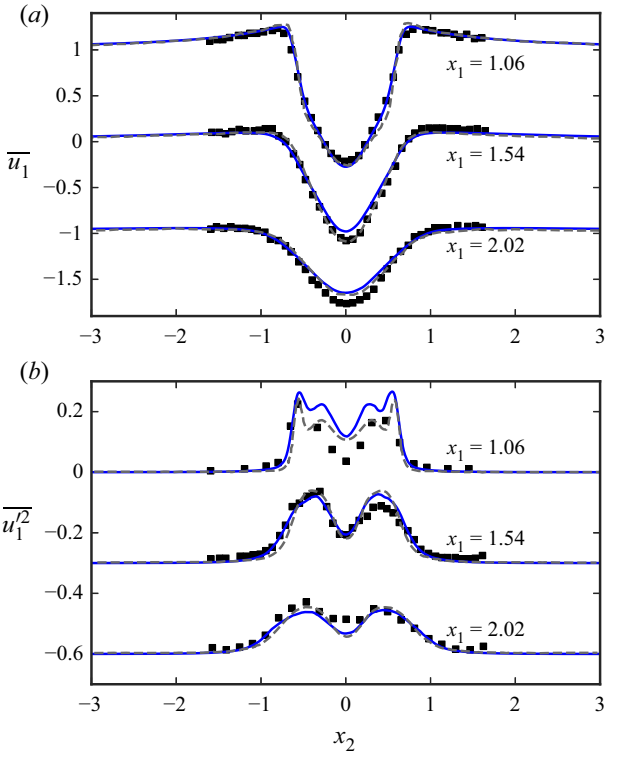

Figure 18. (*a*) Mean streamwise component $\overline{u_1}$ of velocity and (*b*) the average $\overline{u_1'^2}$ of the square of the streamwise fluctuation velocity as functions of x_2. Blue solid lines, the present DNS results ($Re_D = 5000$) at $x_1 = 1.06$, 1.54 and 2.02; grey dotted lines, DNS ($Re_D = 3900$) by Ma, Karamanos & Karniadakis (2000); black squares, experimental data ($Re_D = 3900$) by Lourenco & Shih (personal communication 1994) (data can be found in Beaudan & Moin (1995) and Ma *et al.* (2000)). We show the results for $x_1 = 1.54$ and 2.02 with vertical shifts.

Supplementary movies. Supplementary movies are available at https://doi.org/10.1017/jfm.2023.824.

Funding. This study was partly supported by the JSPS Grants-in-Aid for Scientific Research 20H02068, 21K20403 and 23K13253. The DNS were conducted by using the computational resources of the supercomputers Flow at Information Technology Center Nagoya University and Fugaku through the HPCI System Research Projects (hp210075 and hp210207). The numerical analyses were conducted under the auspices of the NIFS Collaboration Research Programs (NIFS20KNSS145 and NIFS22KISS010).

Declaration of interests. The authors report no conflict of interest.

Author ORCIDs.
Yutaro Motoori https://orcid.org/0000-0002-9647-9014;
Susumu Goto https://orcid.org/0000-0001-7013-7967.

Appendix A. Validations

To validate the DNS results, we define the mean velocity as

$$\overline{u_i}(x_1, x_2) = \frac{1}{TL_z}\int_0^T \int_0^{L_z} u_i(\boldsymbol{x}, t)\,\mathrm{d}x_3\,\mathrm{d}t \tag{A1}$$

https://doi.org/10.1017/jfm.2023.824 Published online by Cambridge University Press

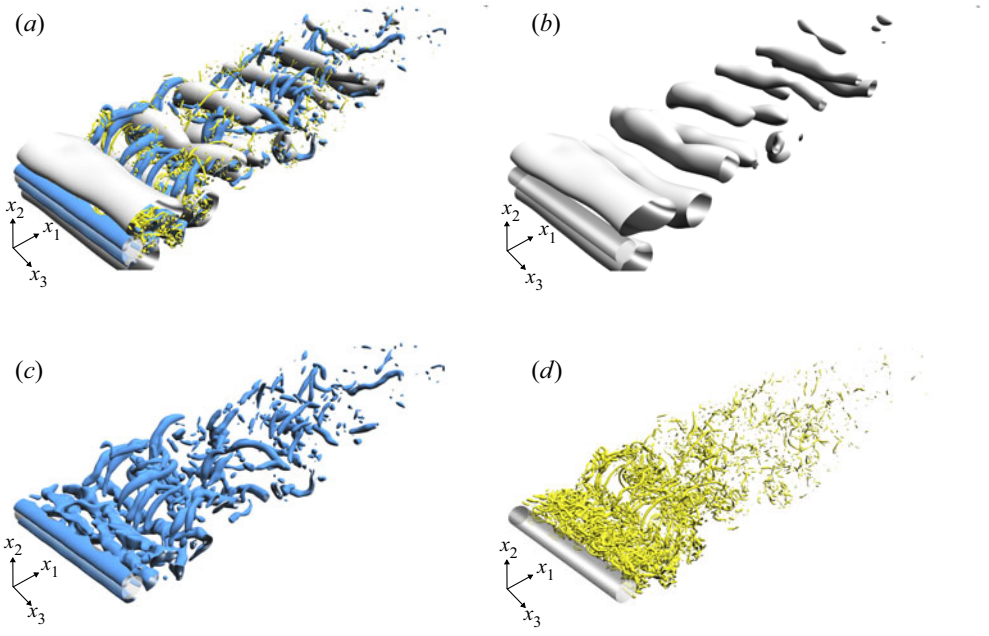

Figure 19. Coherent vortices with veracious sizes in the turbulent wake with quasi-stationary shedding vortices. (*b–d*) Isosurfaces of the second invariant $Q^{(\sigma)}$ of the scale-decomposed velocity gradient tensor with (*b*) filter scale $\sigma = \sigma_{max}$, (*c*) $\sigma_{max}/4$ and (*d*) $\sigma_{max}/16$. We set the thresholds: (*b*) 5.0×10^{-3}, (*c*) 1.0×10^{-1} and (*d*) 2.0. In (*a*) we superimpose the vortices identified in (*b–d*).

in time and the axial direction and its fluctuation as

$$u_i'(\boldsymbol{x}, t) = u_i(\boldsymbol{x}, t) - \overline{u_i}(x_1, x_2). \tag{A2}$$

We compare in figure 18(*a*) the present results of the mean streamwise velocity $\overline{u_1}(x_1, x_2)$ with experiments by Lourenco & Shih (personal communication 1994) (data can be found in Beaudan & Moin (1995) and Ma *et al.* (2000)) and DNS by Ma *et al.* (2000) at three streamwise locations: $x_1 = 1.06$, 1.54 and 2.02. Note that the Reynolds number ($Re_D = 5000$) for the present case is similar to the previous one ($Re_D = 3900$). The present results are in good agreement with previous experimental and DNS data, although we observe some discrepancy at $x_1 = 1.06$ probably because of the difference in the Reynolds numbers. Figure 18(*b*) shows the comparison of the x_2 dependence of the average $\overline{u_1'^2}(x_1, x_2)$ of the squared streamwise component of the fluctuation velocity at the three streamwise locations. The present results reasonably agree with the existing data. This justifies the grid resolution of the present DNS.

Appendix B. Hierarchy of coherent vortices with quasi-stationary vortices

We visualize in figure 19 the hierarchy of vortices by using the isosurfaces of $Q^{(\sigma)}$ (2.9) evaluated from $u_i^{(\sigma)}$ without the Reynolds decomposition. Panel (*a*) shows vortices identified by $Q^{(\sigma)}$ at scales $\sigma = \sigma_{max}$, $\sigma_{max}/4$ and $\sigma_{max}/16$, which are visualized separately in panels (*b–d*). We see in panel (*b*) a pair of vortices attached to both sides of the cylinder, which are not identified by $Q'^{(\sigma)}$ (see figure 3*b*). We can also see in panels (*a*,*c*) that their cores can be identified by the isosurfaces of $Q^{(\sigma)}$ at $\sigma = \sigma_{max}/4$. This is the reason why

https://doi.org/10.1017/jfm.2023.824 Published online by Cambridge University Press

we use the scale $\sigma = \sigma_{max}/4$ to identify the quasi-stationary vortices in §§ 3.2 and 4.2. On the other hand, smaller vortices are similar in the two cases with $Q^{(\sigma)}$ and $Q'^{(\sigma)}$.

References

Aasland, T.E., Pettersen, B., Andersson, H.I. & Jiang, F. 2022 Revisiting the reattachment regime: a closer look at tandem cylinder flow at $Re = 10\,000$. *J. Fluid Mech.* **953**, A18.

Aljure, D.E., Lehmkhul, O., Rodríguez, I. & Oliva, A. 2017 Three dimensionality in the wake of the flow around a circular cylinder at Reynolds number 5000. *Comput. Fluid* **147**, 102–118.

Alves Portela, F., Papadakis, G. & Vassilicos, J.C. 2017 The turbulence cascade in the near wake of a square prism. *J. Fluid Mech.* **825**, 315–352.

Alves Portela, F., Papadakis, G. & Vassilicos, J.C. 2020 The role of coherent structures and inhomogeneity in near-field interscale turbulent energy transfers. *J. Fluid Mech.* **896**, A16.

Amsden, A.A. & Harlow, F.H. 1970 A simplified mac technique for incompressible fluid flow calculations. *J. Comput. Phys.* **6**, 322–325.

Aoyama, T., Ishihara, T., Kaneda, Y., Yokokawa, M., Itakura, K. & Uno, A. 2005 Statistics of energy transfer in high-resolution direct numerical simulation of turbulence in a periodic box. *J. Phys. Soc. Japan* **74**, 3202–3212.

Beaudan, P. & Moin, P. 1995 *Numerical Experiments on the Flow Past a Circular Cylinder at Sub-Critical Reynolds Number*. Stanford University.

Borue, V. & Orszag, S.A. 1998 Local energy flux and subgrid-scale statistics in three-dimensional turbulence. *J. Fluid Mech.* **366**, 1–31.

Breuer, M. 1998 Large eddy simulation of the subcritical flow past a circular cylinder: numerical and modeling aspects. *Intl J. Numer. Meth. Fluids* **28**, 1281–1302.

Carbone, M. & Bragg, A.D. 2020 Is vortex stretching the main cause of the turbulent energy cascade? *J. Fluid Mech.* **883**, R2.

Cardesa, J.I., Alberto, V.-M. & Jiménez, J. 2017 The turbulent cascade in five dimensions. *Science* **357**, 782–784.

Cerutti, S. & Meneveau, C. 1998 Intermittency and relative scaling of subgrid-scale energy dissipation in isotropic turbulence. *Phys. Fluids* **10**, 928–937.

Chan, C.I., Schlatter, P. & Chin, R.C. 2021 Interscale transport mechanisms in turbulent boundary layers. *J. Fluid Mech.* **921**, A13.

Chen, Q., Chen, S., Eyink, G.L. & Holm, D.D. 2003 Intermittency in the joint cascade of energy and helicity. *Phys. Rev. Lett.* **90**, 214503.

Cimarelli, A., De Angelis, E. & Casciola, C.M. 2013 Paths of energy in turbulent channel flows. *J. Fluid Mech.* **715**, 436–451.

Cimarelli, A., De Angelis, E., Jiménez, J. & Casciola, C.M. 2016 Cascades and wall-normal fluxes in turbulent channel flows. *J. Fluid Mech.* **796**, 417–436.

Corrsin, S. 1958 Local isotropy in turbulent shear flow. *NACA Tech. Rep.* RM 58B11.

Doan, N.A., Swaminathan, N., Davidson, P.A. & Tanahashi, M. 2018 Scale locality of the energy cascade using real space quantities. *Phys. Rev. Fluids* **3**, 084601.

Domaradzki, J.A. & Rogallo, R.S. 1990 Local energy transfer and nonlocal interactions in homogeneous, isotropic turbulence. *Phys. Fluids* A **2**, 413–426.

Forouzi Feshalami, B., He, S., Scarano, F., Gan, L. & Morton, C. 2022 A review of experiments on stationary bluff body wakes. *Phys. Fluids* **34**, 011301.

Gomes-Fernandes, R., Ganapathisubramani, B. & Vassilicos, J.C. 2015 The energy cascade in near-field non-homogeneous non-isotropic turbulence. *J. Fluid Mech.* **771**, 676–705.

Goto, S. 2008 A physical mechanism of the energy cascade in homogeneous isotropic turbulence. *J. Fluid Mech.* **605**, 355–366.

Goto, S. 2012 Coherent structures and energy cascade in homogeneous turbulence. *Prog. Theor. Phys. Suppl.* **195**, 139–156.

Goto, S., Saito, Y. & Kawahara, G. 2017 Hierarchy of antiparallel vortex tubes in spatially periodic turbulence at high Reynolds numbers. *Phys. Rev. Fluids* **2**, 064603.

Hamba, F. 2015 Turbulent energy density and its transport equation in scale space. *Phys. Fluids* **27**, 085108.

Hamba, F. 2019 Inverse energy cascade and vortical structure in the near-wall region of turbulent channel flow. *Phys. Rev. Fluids* **4**, 114609.

Hill, R.J. 2002 Exact second-order structure-function relationships. *J. Fluid Mech.* **468**, 317–326.

Hirota, M., Nishio, Y., Izawa, S. & Fukunishi, Y. 2020 Hierarchical vortical structures extracted from turbulent fields. *Fluid Dyn. Res.* **52**, 015503.

https://doi.org/10.1017/jfm.2023.824 Published online by Cambridge University Press

HONG, J., KATZ, J., MENEVEAU, C. & SCHULTZ, M.P. 2012 Coherent structures and associated subgrid-scale energy transfer in a rough-wall turbulent channel flow. *J. Fluid Mech.* **712**, 92–128.

HWANG, J., LEE, J., SUNG, H.J. & ZAKI, T.A. 2016 Inner-outer interactions of large-scale structures in turbulent channel flow. *J. Fluid Mech.* **790**, 128–157.

JOHNSON, P.L. 2021 On the role of vorticity stretching and strain self-amplification in the turbulence energy cascade. *J. Fluid Mech.* **922**, A3.

KAJISHIMA, T. & TAIRA, K. 2017 *Computational Fluid Dynamics*. Springer.

KAWATA, T. & ALFREDSSON, P.H. 2018 Inverse interscale transport of the Reynolds shear stress in plane Couette turbulence. *Phys. Rev. Lett.* **120**, 244501.

KAWATA, T. & ALFREDSSON, P.H. 2019 Scale interactions in turbulent rotating planar Couette flow: insight through the Reynolds stress transport. *J. Fluid Mech.* **879**, 255–295.

KEMPE, T. & FRÖHLICH, J. 2012 An improved immersed boundary method with direct forcing for the simulation of particle laden flows. *J. Comput. Phys.* **231**, 3663–3684.

KIDA, S. & MIURA, H. 1998 Identification and analysis of vortical structures. *Eur. J. Mech. (*B*/Fluids)* **17**, 471–488.

KOBAYASHI, H. 2005 The subgrid-scale models based on coherent structures for rotating homogeneous turbulence and turbulent channel flow. *Phys. Fluids* **17**, 045104.

KOBAYASHI, H., HAM, F. & WU, X. 2008 Application of a local SGS model based on coherent structures to complex geometries. *Intl J. Heat Fluid Flow* **29**, 640–653.

LEE, J., LEE, J.H., CHOI, J.I. & SUNG, H.J. 2014 Spatial organization of large- and very-large-scale motions in a turbulent channel flow. *J. Fluid Mech.* **749**, 818–840.

LEE, J., SUNG, H.J. & ZAKI, T.A. 2017 Signature of large-scale motions on turbulent/non-turbulent interface in boundary layers. *J. Fluid Mech.* **819**, 165–187.

LEHMKUHL, O., RODRÍGUEZ, I., BORRELL, R., CHIVA, J. & OLIVA, A. 2014 Unsteady forces on a circular cylinder at critical Reynolds numbers. *Phys. Fluids* **26**, 125110.

LEHMKUHL, O., RODRÍGUEZ, I., BORRELL, R. & OLIVA, A. 2013 Low-frequency unsteadiness in the vortex formation region of a circular cylinder. *Phys. Fluids* **25**, 085109.

LEUNG, T., SWAMINATHAN, N. & DAVIDSON, P.A. 2012 Geometry and interaction of structures in homogeneous isotropic turbulence. *J. Fluid Mech.* **710**, 453–481.

LIN, C.L. 1999 Near-grid-scale energy transfer and coherent structures in the convective planetary boundary layer. *Phys. Fluids* **11**, 3482–3494.

LIN, J.C., VOROBIEFF, P. & ROCKWELL, D. 1996 Space-time imaging of a turbulent near-wake by high-image-density particle image cinematography. *Phys. Fluids* **8**, 555–564.

LOZANO-DURÁN, A., HOLZNER, M. & JIMÉNEZ, J. 2016 Multiscale analysis of the topological invariants in the logarithmic region of turbulent channels at a friction Reynolds number of 932. *J. Fluid Mech.* **803**, 356–394.

MA, X., KARAMANOS, G.-S. & KARNIADAKIS, G.E. 2000 Dynamics and low-dimensionality of a turbulent near wake. *J. Fluid Mech.* **410**, 29–65.

MARATI, N., CASCIOLA, C.M. & PIVA, R. 2004 Energy cascade and spatial fluxes in wall turbulence. *J. Fluid Mech.* **521**, 191–215.

MARUSIC, I. & MONTY, J.P. 2019 Attached eddy model of wall turbulence. *Annu. Rev. Fluid Mech.* **51**, 49–74.

MCKEOWN, R., OSTILLA-MÓNICO, R., PUMIR, A., BRENNER, M.P. & RUBINSTEIN, S.M. 2018 Cascade leading to the emergence of small structures in vortex ring collisions. *Phys. Rev. Fluids* **3**, 124702.

MCKEOWN, R., OSTILLA-MÓNICO, R., PUMIR, A., BRENNER, M.P. & RUBINSTEIN, S.M. 2020 Turbulence generation through an iterative cascade of the elliptical instability. *Sci. Adv.* **6**, eaaz2717.

MIURA, H. & KIDA, S. 1997 Identification of tubular vortices in turbulence. *J. Phys. Soc. Japan* **66**, 1331–1334.

MOTOORI, Y. & GOTO, S. 2019 Generation mechanism of a hierarchy of vortices in a turbulent boundary layer. *J. Fluid Mech.* **865**, 1085–1109.

MOTOORI, Y. & GOTO, S. 2020 Hairpin vortices in the largest scale of turbulent boundary layers. *Intl J. Heat Fluid Flow* **86**, 108658.

MOTOORI, Y. & GOTO, S. 2021 Hierarchy of coherent structures and real-space energy transfer in turbulent channel flow. *J. Fluid Mech.* **911**, A27.

MOTOORI, Y., WONG, C. & GOTO, S. 2022 Role of the hierarchy of coherent structures in the transport of heavy small particles in turbulent channel flow. *J. Fluid Mech.* **942**, A3.

NATRAJAN, V.K. & CHRISTENSEN, K.T. 2006 The role of coherent structures in subgrid-scale energy transfer within the log layer of wall turbulence. *Phys. Fluids* **18**, 065104.

https://doi.org/10.1017/jfm.2023.824 Published online by Cambridge University Press

NORBERG, C. 2003 Fluctuating lift on a circular cylinder: review and new measurements. *J. Fluids Struct.* **17**, 57–96.

OHKITANI, K. & KIDA, S. 1992 Triad interactions in a forced turbulence. *Phys. Fluids* A **4**, 794–802.

ONG, L. & WALLACE, J. 1996 The velocity field of the turbulent very near wake of a circular cylinder. *Exp. Fluids* **20**, 441–453.

PARNAUDEAU, P., CARLIER, J., HEITZ, D. & LAMBALLAIS, E. 2008 Experimental and numerical studies of the flow over a circular cylinder at Reynolds number 3900. *Phys. Fluids* **20**, 085101.

PIOMELLI, U., YU, Y. & ADRIAN, R.J. 1996 Subgrid-scale energy transfer and near-wall turbulence structure. *Phys. Fluids* **8**, 215–224.

RAJAGOPALAN, S. & ANTONIA, R.A. 2005 Flow around a circular cylinder—structure of the near wake shear layer. *Exp. Fluids* **38**, 393–402.

RODRÍGUEZ, I., LEHMKUHL, O., CHIVA, J., BORRELL, R. & OLIVA, A. 2015 On the flow past a circular cylinder from critical to super-critical Reynolds numbers: wake topology and vortex shedding. *Intl J. Heat Fluid Flow* **55**, 91–103.

SILVA, T.S., ZECCHETTO, M. & DA SILVA, C.B. 2018 The scaling of the turbulent/non-turbulent interface at high Reynolds numbers. *J. Fluid Mech.* **843**, 156–179.

SIMENS, M.P., JIMÉNEZ, J., HOYAS, S. & MIZUNO, Y. 2009 A high-resolution code for turbulent boundary layers. *J. Comput. Phys.* **228**, 4218–4231.

TAO, B., KATZ, J. & MENEVEAU, C. 2002 Statistical geometry of subgrid-scale stresses determined from holographic particle image velocimetry measurements. *J. Fluid Mech.* **457**, 35–78.

THOMPSON, M.C. & HOURIGAN, K. 2005 The shear-layer instability of a circular cylinder wake. *Phys. Fluids* **17**, 021702.

UHLMANN, M. 2005 An immersed boundary method with direct forcing for the simulation of particulate flows. *J. Comput. Phys.* **209**, 448–476.

VELA-MARTÍN, A. 2022 Subgrid-scale models of isotropic turbulence need not produce energy backscatter. *J. Fluid Mech.* **937**, A14.

WATANABE, T., DA SILVA, C.B. & NAGATA, K. 2019 Non-dimensional energy dissipation rate near the turbulent/non-turbulent interfacial layer in free shear flows and shear free turbulence. *J. Fluid Mech.* **875**, 321–344.

WATANABE, T., DA SILVA, C.B. & NAGATA, K. 2020 Scale-by-scale kinetic energy budget near the turbulent/nonturbulent interface. *Phys. Rev. Fluids* **5**, 124610.

WATANABE, T., SAKAI, Y., NAGATA, K., ITO, Y. & HAYASE, T. 2014 Vortex stretching and compression near the turbulent/non-turbulent interface in a planar jet. *J. Fluid Mech.* **758**, 754–785.

WILLIAMSON, C.H.K. 1996 Vortex dynamics in the cylinder wake. *Annu. Rev. Fluid Mech.* **28** (1), 477–529.

YAO, H., MOLLICONE, J.P. & PAPADAKIS, G. 2022 Analysis of interscale energy transfer in a boundary layer undergoing bypass transition. *J. Fluid Mech.* **941**, A14.

YAO, J. & HUSSAIN, F. 2022 Vortex reconnection and turbulence cascade. *Annu. Rev. Fluid Mech.* **54**, 317–347.

YASUDA, T., GOTO, S. & VASSILICOS, J.C. 2020 Formation of power-law scalings of spectra and multiscale coherent structures in the near-field of grid-generated turbulence. *Phys. Rev. Fluids* **5**, 014601.

YASUDA, T. & VASSILICOS, J.C. 2018 Spatio-temporal intermittency of the turbulent energy cascade. *J. Fluid Mech.* **853**, 235–252.

YONEDA, T., GOTO, S. & TSURUHASHI, T. 2022 Mathematical reformulation of the Kolmogorov–Richardson energy cascade in terms of vortex stretching. *Nonlinearity* **35**, 1380–1401.

ZHOU, Y., NAGATA, K., SAKAI, Y., WATANABE, T., ITO, Y. & HAYASE, T. 2020 Energy transfer in turbulent flows behind two side-by-side square cylinders. *J. Fluid Mech.* **903**, A4.

https://doi.org/10.1017/jfm.2023.824 Published online by Cambridge University Press